Extracting Atmospheric Parameters from spectrometer measurements and comparison with established methods

Master's Thesis in Physics

Author:

Joanna Janas

28. April 2017

Friedrich-Alexander University Erlangen Nuremberg
German Aerospace Center (DLR)

Supervisor: Prof. Dr. Gerd Leuchs (FAU)
Co-Supervisor: Dr. Peter Gege (DLR), Sebastian Riedel (EOM)

Abstract

The main goal of the master thesis is the examination of a measurement concept and evaluation method for extracting aerosol parameters from measurements with any spectrometer comparable to established sun photometer method.

Contents

1 Introduction

Remote sensing is the acquisition of electromagnetic radiation propagating from the direction of the earth's surface with satellite or airborne sensors. The light which gets reflected from the surface undergoes significant interaction with the atmosphere before reaching the sensor (see Figure 1). It is therefore a major challenge for remote sensing applications to separate the contribution of the atmosphere from the surface reflectance. Atmospheric correction technique are a major issue in visible or near-infrared (NIR) remote sensing, especially over water. One of the main optical characteristics of the atmosphere is the optical thickness which depends on the atmospheric turbidity, spectral and vertical distribution of the total aerosol load, their composition and relative humidity. Considering their spatial and temporal variability of atmospheric aerosols makes the atmospheric correction a challenging task. The contribution of light scattering by molecules (Rayleigh scattering) is well understood and can be subtracted from the top-of-atmosphere radiance. The aerosol properties have to be separated from the surface reflectance simultaneously leading to development of various atmospheric correction algorithms [1]. Over ocean the contribution from surface in the IR range is very small due to the high absorption of NIR light of water. Consequently any detected signal originates from contribution of the atmosphere. This technique is known as the black pixel approach [2]. Using pre-calculated look-up tables aerosol properties like aerosol optical depth (AOD) can be derived. By making use of the Ångström formula the aerosol optical depth can be extended to the visible wavelength range. Currently different atmospheric correction algorithms are applied to different scenarios like oceans or terrestrial grounds. One of the main efforts is to develop a unified algorithm to cope with all possible scenarios [3]. Nevertheless for coastal regions and shallow or very turbid water, the so called case-2 water scenario [1], atmospheric corrections faces unresolved problems [4, 5]. To further enhance and optimize atmospheric correction algorithms ground based in-situ measurements are required. In-situ measurements are preformed to provide aerosol parameters which are used to validate aerosol parameter retrieved by remote sensing data from satellites and airborne sensors. In-situ parameters serve as input to atmospheric correction algorithms.

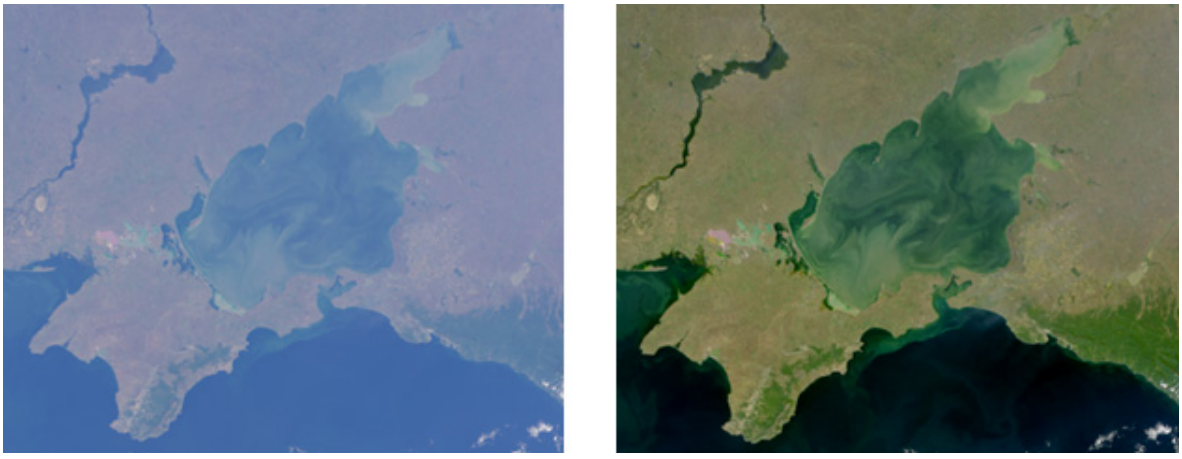

Figure 1: Azof Sea captured by Sea-viewing Wide Field-of-view Sensor (SeaWiFS). On the left side is the original image and on the right side an atmospheric correction algorithms was applied. The influence of the atmosphere can be easily seen. Image taken from [6]

In general sun photometers are the established and commonly used instruments for ground-based

in-situ aerosol parameter retrieval. These instruments measure the direct solar radiance by capturing the radiance signal of the solar disk. For reliable measurement results a small field of view (FOV), diffuse light rejection and a accurate calibration are required. The remote sensing community performes field experiments with a variety of instruments. To ensure data quality and reliable interpretation of results these measurements have to be validated. Thus comparisons between retrieval methods and remote sensing instruments are inevitable and various studies have been conducted on this scope [7, 8, 9]. To ensure comparable measurement results sun photometer networks like AERONET [10], Pandonia and ESR (SKYNET) have been established to provide scientists and institutes with near real-time data of aerosol properties extracted by sun photometer which are identically calibrated, operated and processed. These sun photometers are equally distributed all over the world. Nevertheless due to the spatial and temporal variability of aerosols on regional scale atmospheric parameters extracted by these networks may be not valid for field experiments taking place at regions e.g. lakes or coastal regions not covered by the mentioned networks. Since spectrometers are widely used in the remote sensing community the goal of this thesis is the development of an alternative measurement concept performed with a spectrometer with suitable spectral range and resolution. Instead of the direct solar irradiance measured by sun photometers the total downwelling irradiance and diffuse irradiance are measured and their ratio is calculated. Methods taking advantage of irradiance ratios have been developed in the past [11]. Measuring a broad spectral range the evaluation method is based on a simple analytic radiative transfer model containing aerosol parameters, ozone and water vapor. To verify the reliability of this measurement concept it is validated in respect to the sun photometer network AERONET and the hand-held sun photometers device Microtops II.

2 Theoretical Background

To understand the operational and retrieval techniques of the used instruments a theoretical background about radiative processes and optical properties of aerosols are presented. In this section first the radiative transfer model and analytic spectral atmospheric radiative transfer model as a different modeling approach will be explained. Then a general explanation of the optical properties characterizing aerosol particles follows. A a rough classification of aerosol types and models is presented afterwards. Aerosols refer to colloidal systems of atmospheric particles with an internal liquid and solid structure which differ and are classified by their chemical composition, concentration, size and shape. Aerosol are divided into primary and secondary aerosols ranging in size from a few nanometers to several tens of micrometers [12, 13, 14]. Primary aerosols like sea-salt and dust enter the atmosphere directly from the surface, whereas secondary aerosols are generated by gas-to-particle conversions in the atmosphere. Due to their interaction with cloud droplets, ice crystals, gases and aerosol particles themselves the study of aerosols is of great importance for cloud physics, atmospheric sciences and climate modeling.

2.1 Radiative Transfer Equation

The radiative transfer equation (RTE) describes the conservation of energy for a beam of radiance propagating through absorbing, scattering atmospheric medium. The RTE is expressed by the following formula:

$$\vec{n}\vec{\nabla} I_t(\vec{r},\vec{n}) = -\kappa_{ext} I_t(\vec{r},\vec{n}) + \kappa_{sca}\int_{4\pi} P(\vec{n'},\vec{n}) I_t(\vec{r},\vec{n'}) d\vec{n'} + S(\vec{r},\vec{n}) \tag{1}$$

$$I_t \quad \text{in} \quad \left[\frac{W}{m^2 \cdot nm \cdot sr}\right] \tag{2}$$

The parameter $\vec{r}$ represents the radius vector of the observation point and $\vec{n}$ the direction of the incident beam. The first part of the equation expresses the loss due to extinction of the radiant beam I_t. It is assumed that the change in radiance propagation through the medium is proportional to the incident radiance. For simplification the medium is considered isotropic and there is no nonlinear dependence in the extinction coefficient $\kappa_{ext}(I_t)$. The second term represents the accounts for scattering from all other direction into the beam since ambient radiance may be passing through the scattering volume. The term $S(\vec{r},\vec{n})$ refer to thermal radiation sources. The phase function $P(\vec{n'},\vec{n})$ describes the strength of scattered light from direction $\vec{n'}$ to the direction $\vec{n}$ by aerosol particle. Polarization is neglected by this formula. In this case the Vector Radiative Transfer Equation (VRTE) provides a more accurate theory. (REFERENCE) In most applications considering optical engineering, areas of applied optics and the current satellite remote sensing of aerosol medium from space the 1-D radiative transfer model due to its general physical dependencies and fast calculation is used. In this cases the inhomogenity of the aerosol medium is neglected and aerosol layer in the horizontal direction is assumed to be infinite. Moreover the geometrical depth is transformed to the optical depth $\tau = \kappa_{ext} z$. The higher-dimensional RTE therefore transforms into the one-dimensional RTE:

$$cos(\theta)\frac{dI(\tau,\theta,\phi)}{d\tau} = -I(\tau,\theta,\phi) + \frac{\omega_0}{4\pi}\int_0^{2\pi} d\phi \int_0^{pi} I(\tau,\theta,\phi) p(\theta) sin\theta d\theta \tag{3}$$

2.2 Analytic Spectral Atmospheric Irradiance Model

In comparison to the described Radiative Transfer Model (RTE and VRTE) a different approach for modelling irradiances has been developed by Bird and Riordan [15]. This model has been further extended for coastal and maritime application and has proven reliable results for atmospheric radiance simulations [16, 17]. It describes a simplified analytic expression for **downwelling irradiance** $\left[\frac{W}{m^2 \cdot nm}\right]$ in which starting from extraterrestrial irradiance corrected for the earth-sun orbital distance the irradiance is attenuated through the atmosphere. In general the irradiance is modelled by the sum of different contributions as Rayleigh scattering, aerosol scattering and direct radiance. Therefore this model is adequate for clear-sky conditions where multiple scattering can be neglected. In this sense the downwelling irradiance E_d splits up into two light source components namely the **direct solar irradiance** E_{dd} and the **diffuse irradiance** E_{ds} arising from scattering in the atmosphere.

$$E_d = E_{dd} + E_{ds} \tag{4}$$

$$\text{with} \quad E_{dd}(\lambda) = F_0(\lambda) cos\theta T_r(\lambda) T_a(\lambda) T_{oz}(\lambda) T_u(\lambda) T_w(\lambda) \tag{5}$$

$$\text{with} \quad E_{ds}(\lambda) = I_r(\lambda) + I_a(\lambda) + I_g(\lambda) \tag{6}$$

The diffuse irradiance component arises from three different contributions of light scattering:

- I_r diffuse component arising from Rayleigh scattering

$$I_r = F_0(\lambda) cos\theta T_{oz} T_u T_w T_{aa} (1 - T_r^{0.95}) 0.5 \tag{7}$$

- I_a diffuse component arising from aerosol scattering

$$I_a = F_0(\lambda) cos\theta T_{oz} T_u T_w T_{aa} T_r^{1.5} (1 - T_{as}) F_a \tag{8}$$

- I_g diffuse component arising from multiple ground-air interactions

$$I_g = (E_{dd} + I_r + I_a)\zeta \quad \text{with} \quad \zeta = r_s r_g / (1 - r_s r_g) \tag{9}$$

  with r_s, r_g being the sky reflectivity and ground albedo

The parameter $F_0(\lambda)$ represents the mean extraterrestrial solar irradiance $H_o(\lambda)$ corrected for earth-sun distance and orbital eccentricity $e = 0.0167$ (D is the day of year):

$$F_0(\lambda) = H_o(\lambda) \left[1 - ecos(2\pi(D-2)/365\right]^2 \tag{10}$$

The angle θ is the sun zenith angle at a given location. The T_i provides the transmittance of the corresponding component i due to scattering and absorption by particles and molecules. Hence solar irradiance is attenuated mainly by processes like scattering on molecules (T_r), absorption by gas mixture like Oxygen (T_o), absorption by ozone (T_{oz}), aerosol contributed scattering (T_{as}) and absorption by aerosols (T_{aa}) (extinction T_a) and absorption by water vapor (T_{wv}).
The transmittance attributed by aerosols relates to the single scattering albedo ω_a and the aerosol optical depth τ_a represented by the Ångström formula (30) which is presented in the following section 2.3:

$$T_{as}(\lambda) = e^{-\omega_a \tau_a M(\theta)} = e^{-\omega_a \beta \lambda^{-\alpha} M(\theta)} \tag{11}$$

$$T_{aa}(\lambda) = e^{-(1-\omega_a)\tau_a M(\theta)} \tag{12}$$

For the single scattering albedo ω_a formula [15] is replaced by an empirical relation presented by Greg and Carder [17] due to its independence on humidity. This relation contains the Air Mass Type AM which ranges from 1 to 10 where 1 represents marine aerosol-conditions and 10 continental aerosol-conditions.

$$\omega_a = (-0.0032AM + 0.972)e^{3.06 \cdot 10^{-4} RH} \tag{13}$$

The atmospheric path length $M(\theta)$ can be calculated with $1/cos\theta$ but this approximation fails at higher zenith angles. For this a more sophisticated formula taking into account the sphericity of the earth atmosphere has to be taken from Young (1994) [18]:

$$M(\theta) = \frac{1.002432cos^2\theta + 0.148386cos\theta + 0.0096467}{cos^3\theta + 0.149864cos^2\theta + 0.0102963cos\theta + 0.000303978} \tag{14}$$

Referring to the aerosol component of the diffuse irradiance (Formula 8) the parameter F_a has to be introduced as the forward scattering probability of the aerosol. Clearly the forward scattering probability has to be a function of the sun zenith angle θ and the asymmetry factor g (Formula 37) to account for the directional dependency of the scattering intensities by aerosols (Figure 2). The formula for F_a derived by Greg and Carder [17] is used which connects both the relation by Bird and Riordan [15] for continental aerosols and the relation for marine aerosols by Shettle and Fenn [19].

$$F_a = 1 - 0.5exp\left[(B_1 + B_2cos\theta)cos\theta\right] \tag{15}$$

$$B_1 = B_3\left[1.459 + B_3(0.1595 + 0.4129B_3)\right] \tag{16}$$

$$B_2 = B_3\left[0.0783 + B_3(-0.3824 - 0.5874B_3)\right] \tag{17}$$

$$B_3 = ln(1 - g) \tag{18}$$

with

$$g = \begin{cases} 0.82, & \text{for } \alpha < 0 \\ -0.1417\alpha + 0.82, & \text{for } 0 < \alpha < 1.2 \\ 0.65, & \text{for } \alpha > 1.2 \end{cases} \tag{19}$$

For the calculation of the Rayleigh transmittance the path length corrected for nonstandard atmospheric pressure $M_c(\theta)$ is important. Moreover the wavelength unit has to be in micrometer [μm]:

$$T_r(\lambda) = e^{-\tau_r(\lambda,\theta)} = e^{\frac{M_c(\theta)}{115.6406\lambda^4 - 1.335\lambda^2}} \quad M_c(\theta) = M(\theta)P/P_\theta \tag{20}$$

The calculation of the transmittances T_{oz}, T_o and T_w requires the mean wavelength dependent absorption coefficients a_{oz}, a_o and a_w. Besides these parameters the atmospheric path length for ozone M_{oz} and the ozone scale height H_{oz} have to be determined [20]. The ozone scale height represents the total amount of ozone in a vertical column under NTP conditions. It is commonly expressed in Dobson Units DU and can be given in cm while 100 DU corresponds to a 1 cm thick layer of ozone. Additionally the Water Vapor WV in cm has to be determined.

$$T_{oz} = exp[-a_{oz}(\lambda)H_{oz}M_{oz}(\theta)] \quad \text{with} \quad M_{oz} = \frac{1.0035}{\sqrt{cos^2(\theta) + 0.007}} \tag{21}$$

$$T_o = exp\left[\frac{-1.41a_o(\lambda)M'(\theta)}{\left[1 + 118.3a_o(\lambda)M'(\theta)\right]^{0.45}}\right] \tag{22}$$

$$T_w = exp\left[\frac{-0.2385 a_w(\lambda) \cdot WV \cdot M(\theta)}{[1 + 20.07 a_w(\lambda) \cdot WV \cdot M(\theta)]^{0.45}}\right] \tag{23}$$

2.3 Optical Properties of Aerosols

In order to investigate the influence of aerosol particles on the attenuation of light intensities during propagation through the atmosphere optical properties defining the scattering and the absorption process are important to understand. Some simplifications have to be made for modeling of aerosol optical properties. These are spherical shape, homogeneity and no coatings of aerosol particles. Different aerosols scatter and absorb sunlight to varying degrees and both the electromagnetic field inside the particle for energy absorption effects and outside can be calculated using Mie Theory. The sum of the scattering in all directions and absorption process is called **extinction**. An important term to describe the extinction process is the **cross-section** which describes how much of the incidents beam intensity is decreased in term of the area of the beam considering an plane electromagnetic wave interaction with an particle. Regarding the scattering process the scattered energy can be integrated with respect to the direction of scattering yielding the scattering cross-section C_{sca} with I_0 as the incident beam intensity and I_{sca} as the intensity of the scattered light and S the area surrounding the particle.

$$C_{sca} = \frac{1}{I_0} \int_S I_{sca} dS \tag{24}$$

Considering absorption effects the absorption cross-section C_{abs} with V as the volume, k as the wave number, $\vec{E_0}$ as the electric vector of the incident wave and $\vec{E}$ inside the scatterer is defined as

$$C_{abs} = \frac{k}{|\vec{E_0}|^2} \int_V |\vec{E}|^2 \epsilon dV. \tag{25}$$

The symbol ϵ defines the dielectric permittivity of the scatterer $\epsilon = 2n\chi$. The parameters n and χ refer to the real and imaginary part of the refractive index $m = n - i\chi$. Thus aerosols particles with an low imaginary part do mainly contribute to the scattering of the light in the atmosphere. According to the World Climate Programme WCP-112 [12] the imaginary part χ of aerosol particles in the visible spectrum is low. In respect to the geometrical cross-section G describing the projection of the particle on the plane perpendicular to the direction of the incident beam both the scattering efficiency and the absorption efficiency factor can be defined as:

$$Q_{sca} = \frac{C_{sca}}{G} \qquad Q_{abs} = \frac{C_{abs}}{G} \quad \text{with} \quad Q_{ext} = Q_{sca} + Q_{abs} \tag{26}$$

Consequently the extinction efficiency factor results from the sum of both factors.
Additional to the efficiency factors their ratio defines the **single scattering albedo** representing the ratio of incoming radiation subject to extinction which is scattered by the particles.

$$SSA = \omega_0 = \frac{Q_{sca}}{Q_{ext}} \tag{27}$$

For highly absorptive particles ω_0 approximates 0 whereas for particles with scattering as the main extinction process the single scattering albedo is close to one.

Extinction Light propagation through the atmosphere leads to an attenuation depending on absorption and scattering coefficients according to the Beer Boguers law:

$$\frac{I_\lambda}{I_{0,\lambda}} = e^{-\kappa_{ext} L} \tag{28}$$

Here $I_\lambda \left[\frac{W}{m^2}\right]$ corresponds to the intensity of the beam which has propagated the distance L through the medium with the extinction coefficient $\kappa_{ext} \left[m^{-1}\right]$ with an initial intensity $I_0 \left[\frac{W}{m^2}\right]$. Integrating the extinction coefficient with the height from the ground level to the top-of-atmosphere h ($\approx$ 60km) results in the aerosol optical thickness (AOT) $\tau(\lambda)$:

$$\tau(\lambda) = \int_0^h \kappa_{ext}(\lambda, z) dz \tag{29}$$

The aerosol optical thickness is a standard parameter measured by AERONET (AErosol RObotic NETwork). To describe the wavelength dependency of the AOT and hence the extinction coefficient of aerosol particles power laws are usually used. The Ångström formula proposed by Ångström in 1929 [21] provides a simplified dependence of the Aerosol Optical Thickness (AOD) or aerosol extinction coefficient on the wavelength.

$$\tau(\lambda) = \beta \lambda^{-\alpha} \quad \text{with} \quad \beta = \tau(550nm) \tag{30}$$

The parameter β represents the turbidity coefficients and equals the aerosol optical thickness either at 1000 nm or 550 nm depending on the definition. In this thesis β will refer to $\lambda = 550$nm which corresponds to the peak in the solar spectrum reaching the top-of-atmosphere. The Ångström exponent α represents the slope of the wavelength dependence of the AOT in logarithmic coordinates and can be deduced with two optical thicknesses at different wavelengths [22, 23].

$$\frac{\tau_1}{\tau_2} = \left(\frac{\lambda_1}{\lambda_2}\right)^{-\alpha} \quad \rightarrow \quad \alpha = -\frac{ln\frac{\tau_1}{\tau_2}}{ln\frac{\lambda_1}{\lambda_2}} \tag{31}$$

The exponent α is a qualitative indicator for the size of the aerosol particles and the fine mode fraction. It can be shown that for values $\alpha > 1.0$ refers to smaller particles as the fine mode or accumulation mode whereas values $\alpha < 1.0$ refers to larger particles comprising the coarse mode though an unambiguous classification can not be guarantied [24]. Additionally a relationship between the Ångström parameters and the aerosol particle size distribution can be shown [25, 26, 27]. One relationship to the power law distribution $n(a) = Aa^{-\gamma}$ with A as normalization constant and a as the particle size was developed by Junge [28]. For spherical particles the extinction absorption coefficient can be expressed by the particle size distribution $n(a)$, the extinction efficiency factor Q_{ext} and the size parameter $x = \frac{2\pi a}{\lambda}$:

$$\kappa_{ext} = \int_{a_1}^{a_2} \pi a^2 Q_{ext}(x, m(\lambda)) n(a) da \tag{32}$$

The size parameter x is a clearer measure of the interested size regime since wavelengths much bigger than the actual particle size do not refract the light in any significant way. The parameter $m(\lambda)$ corresponds to the refractive index. Assuming that the aerosol refractive index is low in the visible and substitution of a by x the integral leads to following relationship between the Ångström exponent α and the Junge power law parameter γ:

$$\alpha = \gamma - 3 \tag{33}$$

Nevertheless it is shown that the Junge law is not often adequate for the description of ambient aerosol distributions that have significant structure [29]. Besides, the Junge power law distribution, the log normal distribution or even multimodal log normal size distributions specifically modeled for sea-salt aerosol seem to correspond to typical size distributions of aerosol [30].

$$n(a) = \frac{1}{\sqrt{2\pi}\sigma a} exp\left\{\frac{ln^2(a/a_0)}{2\sigma^2}\right\} \tag{34}$$

It can be shown that the Ångström exponent α varies with wavelength which is known as the curvature. The curvature provides additional interpretation considering measured aerosol types. Hence it can be shown that the Ångström exponent in the long wavelength regime ($\approx 0.6 - 0.8\mu m$) is sensitive to fine mode volume fraction but not to the fine mode effective radius a_{ef} represented by

$$a_{ef} = \frac{\int_0^\infty a^3 n(a) da}{\int_0^\infty a^2 n(a) da} \tag{35}$$

For the small wavelength regime ($\approx 0.3 - 0.4\mu m$) the opposite case applies [27].

Based on the particle size distribution the extinction of light takes place due to absorption and scattering on aerosol particles. Absorption is mostly due to soot in great amount. On clear sky days the absorptive component of the aerosol particles is small compared to the scattered light. The absorption coefficient based on the particle size distribution and the refractive index can be calculated by the Mie Theory. A more detailed description of the Theory is provided in [31]. Considering the scattering of light by aerosol particles especially the angular distribution of scattered energy for a given local volume of an aerosol medium is of great importance. Figure 2 shows the angular distribution considering Rayleigh scattering on molecules and Mie scattering on aerosol parameters with sizes in the range of incident wavelength. The angular distribution

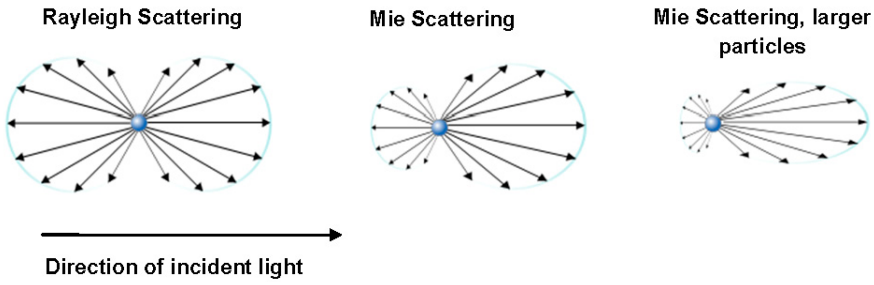

Figure 2: Comparison between Rayleigh and Mie Scattering depending on the ratio of the scatterer to the wavelength of the incident beam (Picture taken from [32])

is described by the closed form Henyes-Greenstein phase function [33]:

$$p(\theta) = \frac{1 - g^2}{(1 + g^2 - 2gcos\theta)^{\frac{3}{2}}} \tag{36}$$

The parameter g refers to the asymmetry parameter

$$g = \frac{1}{2}\int_0^\pi p(\theta) cos\theta sin\theta d\theta \tag{37}$$

defined as the cosine-weighted average of the phase function. The value of the asymmetry parameter ranges from -1 over 0 to 1 corresponding to a backward-scattering, isotrope scattering distribution and froward scattering.

2.4 Aerosol Types and Models

For the purpose of modelling of aerosol optical properties a simplified classification of the aerosols has to be done. Depending on origin aerosol types show remarkable differences in shape and chemical composition (e.g. Picture 3). Considering scattering and absorption processes it is important to define different aerosol types with common attributes to provide reliable forward modelling. Aerosol types are classified according to their origin, shape and chemical composition. Types like sea-salt aerosol (SSA), dust aerosols, secondary aerosols, biological aerosols and anthropogenic aerosols are described in the following. A more detailed description is provided in [13, 14] .

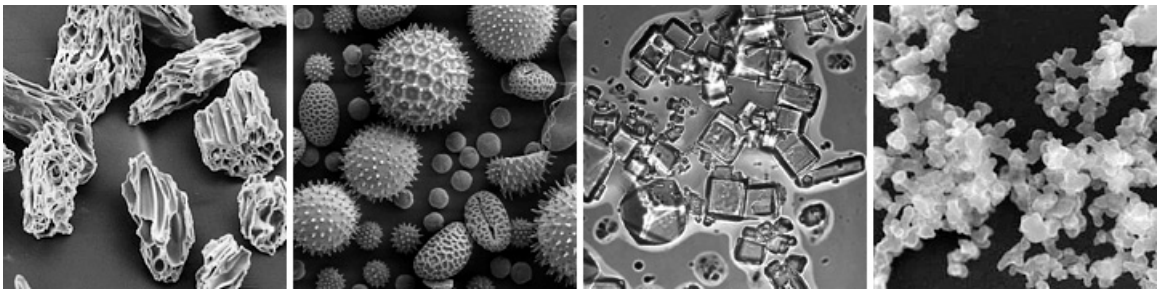

Figure 3: Scanning electron microscope images to show the variety of aerosol shapes. From left to right: volcanic ash, pollen, sea salt and soot.(Micrographs courtesy USGS, UMBC (Cheerer Petty), and Arizona State University (Peter Buseck)). Image taken from [34].

Sea-salt aerosol: The sea-salt aerosol type is an important contributor to the total aerosol load in the atmosphere. The particles are predominantly produced by the oceans surface by wave formation and breaking. Depending on the size and on the meteorological conditions (wind) the particles entrain the atmosphere where they remain for a long time and the sea salt concentration varies approximately linearly with the wind speed [35]. The size ranges typically from 0.1 to 1.0 micrometers and the shape strongly depends on the humidity. In low humidity conditions their shape tends to a cubic structure due to the sodium chloride NaCl. In high humidity conditions spherical crystal shapes can be used as an approximation for sea-salt aerosol particles. At least two aerosol models, the fine and the coarse mode, have to be used to characterize the optical scattering processes of maritime aerosols.

Dust aerosol: These type of aerosols are mostly composed of Silicon (Si). They are not soluble in water and hence does not change drastically with air humidity. The main challenge with dust aerosols origins in the nonsphericity of the shapes and hence the modelling of their optical properties [36]. The inhibit complicated composition and it is difficult to extract the refractive index. Moreover the variability of shapes along the vertical column has to be accounted for and assumption for homogeneity leads to biases [13].

Secondary aerosol: In contrast to primary aerosols which are directly emitted in condensed phase or as semi volatile vapor condensable under atmospheric conditions secondary aerosols are formed by chemical reaction and gas-to-particle conversion of volatile organic compounds [37]. Main components are sulfates SO_4^{2-} from biogenic gases, from volcanic , nitrates NO_3^- and some organics. In general the particles are of spherical shape with size parameters of log normal distribution [13].

Biological aerosol: This type of aerosol contain a great range of particles size and heterogeneity. Viruses $[0.05 - 0.15\mu m]$, bacteria $[0.1 - 4.0\mu m]$, fungal spores $[0.5, 15.0\mu m]$ and pollen $[10.0 - 30.0\mu m]$ belong to this type. Moreover their complex shape and heterogeneity complicates (see Figure 3) the characterization of their optical properties. Additionally the show fluorescence in the ultraviolet light regime[38].

Antropogenic aerosol: This type consists of primary and secondary aerosols like different sulfates, black carbon and carbon oxide. It gained more attention during the past decades indicating higher and higher distribution to the total amount on aerosols. Studies concerning the energy balance of the Earths climate investigate both the cooling and the warming of effect due to anthropogenic aerosols [39]. Sources are anthropogenic biomass burning (forest fires, domestic heating), fossile fuel combustion and industrial emission.

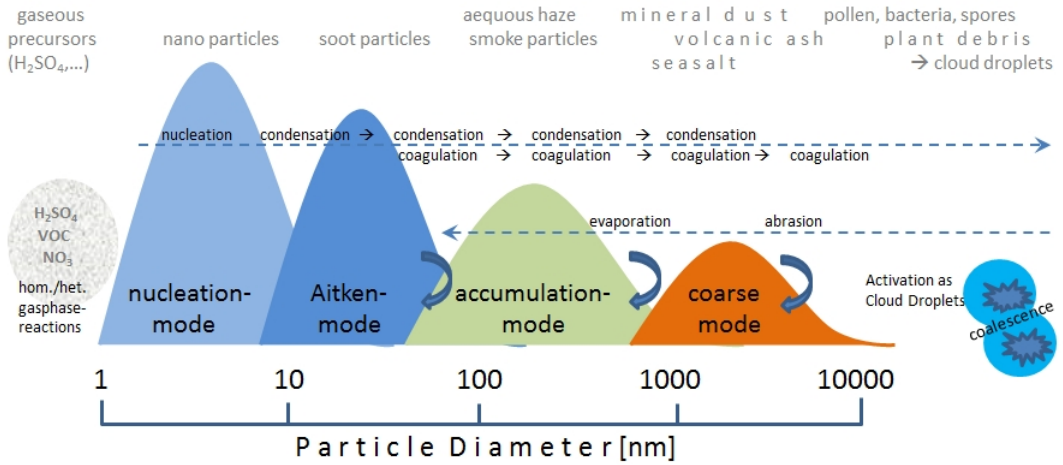

Figure 4: Schematic visualization of particle size distribution with corresponding aerosol types and their conversion processes. Additionally the Nucleation mode for nanometer sized particles is presented here. Image taken from [40].

Since shape properties of specific aerosol types determine the light scattering properties it is important to model the optical properties of aerosols since types and distribution are not known in advance. As mentioned in the description of the different aerosol types a spherical shape of aerosols especially of maritime aerosols is assumed for simpler forward modelling of the scattering processes. In general the sea-salt aerosol is divided into two fractions: the fine mode and the coarse mode depending on the size parameter of the particles [41]. Some research publications tend to define four modes: the Nucleation mode (diameter less than 0.01 μm), the Aitken mode (diameter less than 0.1 μm), the accumulation mode (diameter 0.1 to 2 μm), and the coarse mode (diameter greater than 2 μm). The Nucleation, Aitken and the accumulation mode are referred to fine particles leading to the same result as defined with two mode classification. In Figure (4) the particles size distribution corresponding the different modes with typical transformation

as nucleation, condensation and coagulation are shown. For further reading the Poeschl [37] is recommended. According to this pattern also continental aerosols are divided into such modes. Additionally a classification into water soluble aerosols like sulfates and nitrates and water insoluble aerosol like soil is made. Since this approach does not reflect the scattering process for aerosols with complicated morphologies in e.g. low humidity, efforts in modelling optical processes based on non-spherical aerosols have been studied [42][43]. This affects mainly mineral aerosols and dry sea salt aerosols. Database systems as building blocks for modelling provides various optical properties on the base of chemical properties, refractive index and size distribution of known and well studied aerosol classes [44].

3 Methods

3.1 Ground-based Instruments

In this section the instruments used for the atmospheric radiance measurements are introduced. Ground-based measurement techniques are separated into passive and active techniques. Active remote-sensing techniques like Lidar does not use solar light but signals for light sources to investigate the aerosol medium and the vertical column profile of aerosols by means of backscattering of the emitted light. The passive remote-sensing techniques are based on the solar light analysis for investigation of aerosol media. AERONET sunphotometer, SolarLight Microtops sun photometer and Ibsen spectrometer used in this thesis belong to the scope of passive ground-based measurement techniques.

3.1.1 Ibsen Spectrometer

The spectrometer measurements are performed with an Ibsen Freedom VIS FSV-305 spectrometer based on transmission grating. It has an spectral range of 360 - 830 nm, a spectral resolution of $\approx 1.6\,\text{nm/FWHM}$ and numerical aperture of ≈ 0.16. The integrated high sensitivity and low noise back-thinned CCD image Hamamatsu S10420 sensors works with an quantum efficiency between 50-80 % between 300-850 nm and contains 1024×1024 pixels. The Signal-to-Noise ratio is about 750:1. In the Near-Infrared (NIR) region the CCD sensor shows optical etaloning. The CCD sensor does not have any active temperature stabilization thus darkcurrent measurements are necessary to be performed at each measurement step. For field experiments the CCD detector with the grating and electronics are installed into a box. For field experiment aplications the CCD detector with the grating and electronics are installed into a box 5b. The spectrometer provides an USB connection for communication. A fiber connects the spectrometer with an optic 5a.

(a) *(b)*

Figure 5: Ibsen spectrometer. To meet outdoor requirements the ibsen is installed into a box with an USB connecton and a fiber with optic.

3.1.2 SolarLight Microtops II Sunphotometer

Microtops II produced by the enterprise SolarLight is a hand held portable device suitable for field experiments to measure aerosol optical thickness, water vapor and ozone. The sun photometer measures the direct sun irradiance at five accurately aligned optical collimators with a field of view FOV of approximately 2.5 °. The standard wavelengths with adequate bandpass filters are 340 nm, 380 nm, 440 nm, 500 nm, 675 nm, 870 nm, 936 nm and 1020 nm with a FWHM of 10.0 nm [45]. During measurement the sun photometer has to be pointed directly to the sun

by means of a projected pointing sun target window on the instrument (see Figure 6b). The pointing accuracy to the sun can move up to 1 ° [46] during field experiments. An algorithm to enhance sun targeting accuracy is implemented which scans a series of measurements removing outliers.

(a) *(b)*

Figure 6: (a) CIMEL sun photometers for principal plane and almucantar plane installed on the roof of the Meteorological Institut of Munich (MIM). (b) Hand held Microtops II Sunphotometer with sun target window to point directly to the sun.

3.1.3 AERONET

To enable and provide access to regional ground-based observations of aerosol and water vapor a network of sun photometers called AERONET (AErosol RObotic NETwork) was established by NASA, PHOTONS (PHOtométrie pour le Traitement Opérationnel de Normalisation Satellitaire), CNES and CNRS-INSU [10]. This large AERONET system runs on NASA's Goddard Space Flight Center is expanded by federated networks like RIMA, AeroSpan, AEROCAN, and CARSNET. This network is comprised of more than 200 carefully calibrated and automatically working CIMEL Electronique 318A Sun-sky scanning spectral radiometers placed over the entire world to provide spatial coverage of aerosol measurements (see Figure 7). With the AERONET program a centralized processing and public domain database is given to access and download continuously data from aerosol monitoring for research and validation of satellite aerosol optical property retrievals. The Sun photometers work in an automated environment doing both direct sun measurements and diffuse sky measurements with several programmed sequences. Concerning sky radiance measurements both the solar principal plane with holding the azimuth angle constant and varying the zenith angle and the almucantar plane with holding the zenith angle constant and varying the azimuth angle are measured (see Figure 6a). The measurements start at the early morning and ends at the evening at an air mass of 7. With a filter wheel spectral measurements at the wavelengths (channels) 340, 380, 440, 500, 670, 870, 940 and 1020 nm are taken for

the direct sun measurements. For the sky radiance four spectral bands namely 440, 670, 870 and 1020 nm are measured. The fully field of view angel is 1.2 degrees. During extinction measurements scattered radiation of the diffuse sky light enters the instrument field of fiew (FOV). To minimize the scattered radiation the field of view should be comparable to the solar dis angular dimension. Details of the hardware and functionality are provided in Holben, 1981, [10]. AERONET instrumentation of same design and data collection, calibration with accepted calibration techniques at calibrations sites and scientifically published and accepted algorithms for data processing results in an equal and near real-time available data analyses and standardization of measurement and processing allowing multi-year and global scale comparison.

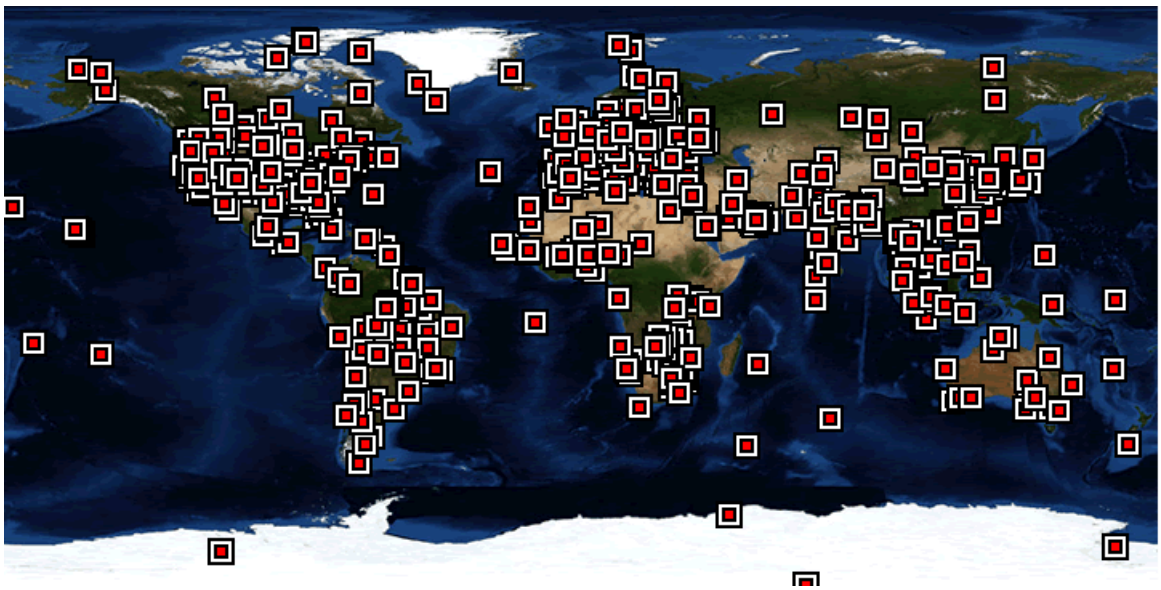

Figure 7: AERONET (Aerosol Robotic Network). Red dots represent sun photometers CIMEL Electronique 318A placed at different locations worldwide. Picture taken from [47]

3.2 Calibration Methods

The analytic radiative transfer model of Greg and Carder [17] models the propagation of light and its attenuation through the atmosphere in terms of the irradiance E. This implies the correct handling of units representing irradiance and radiance (see 3.2).

Quantity	Symbol	Definition	Units
Irradiance	E	$\frac{d\phi}{dA}$	$\frac{mW}{m^2}$
Radiance	L	$\frac{d\phi}{dAd\theta}$	$\frac{mW}{m^2 sr}$

To ensure representative and referable results the calibration of the measurment data according to the spectrometer has to be guaranteed. In this sense it has to be ensured to convert the instrument output from digital number [DN] to radiance $\left[\frac{mW}{m^2 nm \cdot sr}\right]$.

3.2.1 Spectrometer

The spectrometer's output in digital numbers has to be corrected for darkcurrend and nonlinearity and then it has to be converted into the correct physical units by means of a calibrated long term stable reference light source. To characterize the spectrometer one has to execute the so called level zero processing. The result of this processing is to generate characterization values in terms of nonlinearity effects and response of the spectrometer. With both the nonlinearity correction and the response converter subsequent measurement data can be reliable calibrated. To correct for nonlinearity and convert to correct phyiscal units the radiance standard RASTA was used [48].
The calibration setup consists of a white spectralon exhibiting lambertian behavior and a tungsten halogen light bulb as light source (see Figure 8a). To track the stability of the light source intensity five filter radiometers run during the performed measurement.

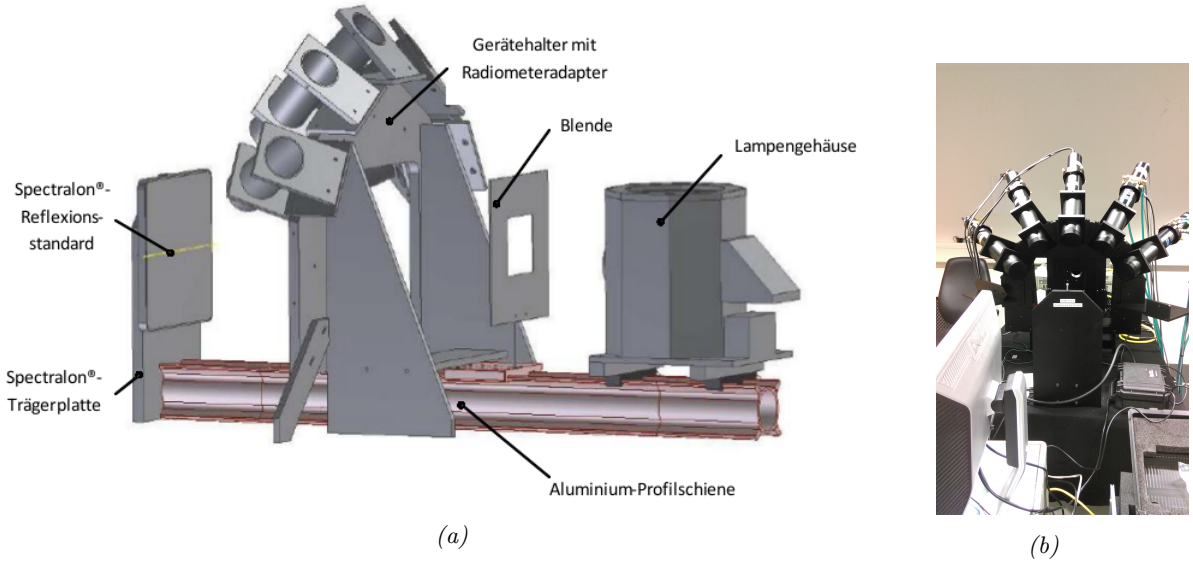

(a) *(b)*

Figure 8: (a) Picture taken from Calibration Certificate. (b) Photograph of RASTA at DLR (Oberpfaffenhofen)

Nonlinearity correction Integrated CCD detector exhibit a non-linearity in response to the light input intensity. That means that the response of a CCD detector does not show a proportional behavior with respect to a monotonically increasing light intensity shining on the CCD detector. Leaving the nonlinearity uncorrected measurements will result in detectable errors in the calculation of normalized values. Various detectors show a different nonlinearity pattern and thus the magnitude varies from detector to detector. In order to correct for nonlinearity the intensity of the reference light source RASTA is kept constant while the integration time of the spectrometer is varied. Then the measured spectra with different integration times are analyzed in the following way. Nonlinearity effects can be seen in deviations of the spectra after the normalization process in respect to integration times. Referring to one channel the plot of [DN]/sec in respect to [DN] would result in a value of one if the CCD detector has no nonlinear effects. During the nonlinearity calibration it is assumed that all pixels are treated equally concerning the nonlinear behavior. Since the calibrated reference light source of RASTA does not show a flat spectrum but different intensities the corresponding normalized spectra has to be additionally normalized to a reference intensity (see table 1 to 3). Then the combined spectra of each channel overlap on a plot of normalized [DN]/sec vs. [DN]. The data is fitted with a spline function $\gamma(S)$ by reducing the least-squares of model and measurement 39. The function $\gamma(S)$ produces correction factors for each intensity input [49]

$$\gamma(S): \quad \text{empirical correction function for signal } S \text{ in [DN]} \tag{38}$$

$$\sum(\gamma\,(S_{k,n}) - \left(\frac{S_{k,n}}{t_n} \cdot \frac{t_{n(\bar{S})}}{\bar{S}}\right))^2 \rightarrow min \quad \forall k{=}Channels, \quad n{=}Exposure\ duration \tag{39}$$

Table 1: A short example describes the nonlinear correction procedure. Assuming the channels on the horizontal columns measure counts which amount is linear to the corresponding integration times in the vertical columns. The values inside the tabe are in [DN].

Integration[ms]:	1	2	4	8	
Channel 1 [DN]	1	2	4	8	
Channel 2 [DN]	2	4	8	16	$\rightarrow$
Channel 3 [DN]	1	2	4	8	

Table 2: To generate a nonlinear correction function $\gamma(\lambda)$ it is necessary to normalize the measurement in respect to an adequate [DN] value and to integration time in [ms].

Integration[ms]:	1	2	4	8	$\frac{t_{n(\bar{S})}}{\bar{S}}$	
Channel 1 [DN]	1	$\boxed{2}$	4	8	$\frac{2}{2}$	$\rightarrow$Divide by $\frac{t_{n(\bar{S})}}{\bar{S}}$ and integration time $\rightarrow$
Channel 2 [DN]	$\boxed{2}$	4	8	16	$\frac{1}{2}$	
Channel 3 [DN]	1	$\boxed{2}$	4	8	$\frac{2}{2}$	

Table 3: The normalized data is then overlap in a plot [DN]/ms vs. [DN]. If the instrument does not inhibit nonlinearity the resulting plot results in a constant of one $\gamma(S)$ as shown in the table. Otherwise slight differences has to be corrected with a function $\gamma(S)$ e.g. spline fit or higher polynomial to correct for the nonlinearity.

Integration[ms]:	1	2	4	8	
Channel 1	1	1	1	1	
Channel 2	1	1	1	1	$\rightarrow \gamma(S) = 1$
Channel 3	1	1	1	1	

The readout signal of CCD detector of the Ibsen Spectrometer is passed to an integrated Analog-to-Digital converter applying an offset gain to avoid negative signal output. Since the thermal noise of the CCD sensor exhibit nonlinear effects (see [50]) one has to ensure to subtract the bias offset of the A/D converter before performing nonlinearity correction.

$$S_{corr} = \frac{S_{raw} - S_{offset}}{\gamma(S_{raw} - S_{offset})} \tag{40}$$

Since the used spectrometer device lacks an active thermal stabilization the darkcurrent signal is measured at two different ambient temperatures, $-3°C$ and $30°C$. The temperature dependence and the gain offset of the spectrometer are not known it advanced. It has to be determined whether the gain offset subtraction is sufficient for correction nonlinearity. Besides the RASTA a second alternative stable light source was set up in the CHB to validate the generated nonlinear correction function.

Darkcurrent subtraction Additional to each measurement a darkcurrent measurement D is taken which has to be subtracted from the measured signal. In the absence of light electrons can be thermally excited from the valence band to the conduction band. Thus the temperature dependence of the darkcurrent $D_{thermal}$ has to be taken into account and temperature stabilization of CCD are commonly used to suppress $D_{thermal}$. It is important to take into account that the darkcurrent does inhibit a nonlinearity f [50]. Additional to the thermally generated contribution the shot noise D_{shot} and the readout noise of the electronics D_{other} belong to the total darkcurrent signal.

$$S_{output} = f(tS_{raw} + D_{thermal} + D_{shot} + D_{other}) + Soffset \tag{41}$$

After nonlinear correction the dark current is subtracted from the received total Signal S.

Radiometric characterization At first the signal has to be normalized to one millisecond $S_0 = \frac{S}{t_{int}}$. The final calibration step is the conversion from digital numbers to the corresponding physical unit. Therefore the measurements taken with RASTA has to equal the calibrated reference data $L_{RASTA}(\lambda)$ of the tungsten halogen light bulb. This can be achieved by simple division of a response factor:

$$S_0 = \frac{S}{r(\lambda)} \quad \text{with} \quad r(\lambda) \quad \text{in} \quad \left[\frac{DN}{\frac{mW}{m^2 nm \cdot sr}}\right] \tag{42}$$

This response factor equals

$$r(\lambda) = \frac{S_{RASTA}(\lambda)}{L_{RASTA}(\lambda)} \tag{43}$$

3.2.2 Level One Processing

Further experimental measurements are calibrated by means of the retrieved nonlinear correction function $\gamma(S)$ and the response factor $r(\lambda)$. It is important that during a measurement procedure both radiance and darkcurrent have to be measured with the same integration time. Then with the corresponding darkcurrent measurement each measurement goes through specific calibration steps. A schematic overview of the calibration processing is described in Figure 9.

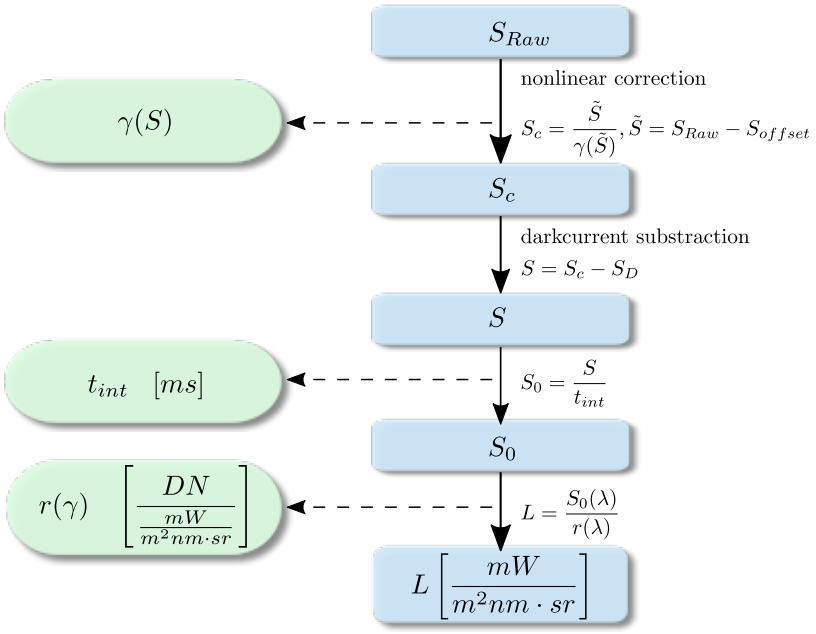

Figure 9: Level 1 processing steps: At first the measured data has to be corrected for nonlinearity. Thus the raw data is divided by the nonlinearity correction $\gamma(S)$ with S in [DN]. After darkcurrent subtraction and normalization to one millisecond the data is converted into adequate physical units. The dotted arrows represents the action "uses".

3.2.3 Microtops SolarLight

Microtops sunphotometer are calibrated using the Langley Method at Izaña Observatory, Teneriffa. Calibration sites with high altitude with stable atmospheric conditions are chosen where regional sources of aerosol are very low. By means of the Langley method the extraterrestrial voltage for the instruments are determined. The signal [DN] is plotted against the optical air mass. The intercept with the y-Axis, the zero air mass, is the corresponding calibration coefficient for the mean extraterrestrial irradiance. The corresponding calibration values can be stored additionally in the instrument.

3.2.4 AERONET

The Aerosol Robotic Network station AERONET is based on nearly yearly inter-calibration of referenced instruments that are calibrated by Langley method at high altitude observations of Mauna loa and Izana every 2-3 month. The field instruments returns to GSFC (Goddard Space Flight Center) for a reference inter comparison. It is advised that field instruments should be re-calibrated every year due to environmental conditions.

3.3 Measurement Procedure and Aerosol Parameter Retrieval

In this section the alternative measurement concept and retrieval of aerosol parameters with spectrometer is presented at first. Instruments like hand held sun photometers are an option for measurement direct sun radiances but require a firm and secure footing for accurate pointing into the direction of the sun. Considering field experiments on boats measuring surface reflectance of water bodies this may be challenging. In the remote sensing community spectrometers are common instruments to measure surface reflectance at field experiments. Thus developing a way to retrieve aerosol parameters by means of spectrometers is a powerful tool to determine atmospheric conditions. In the second part of this section the description of the retrieval method of sun photometer measurement follows.

3.3.1 Ibsen spectrometer

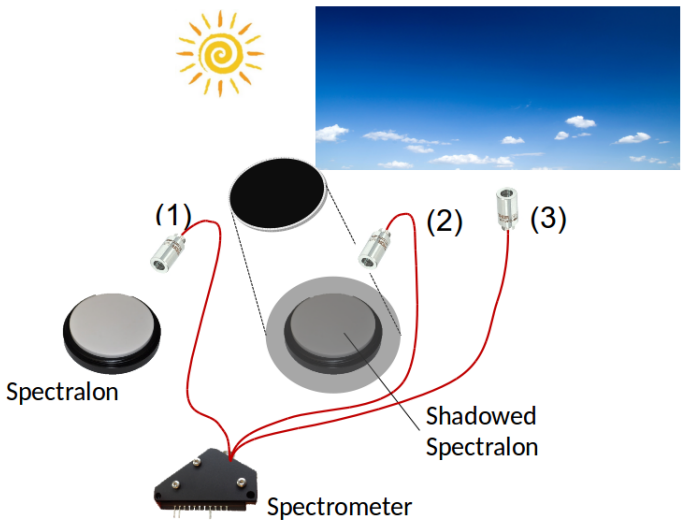

Figure 10: Concept to measure total downwelling irradiance E_d (1), diffuse downwelling irradiance E_{ds} (2) and sky radiance pointing to 0 ° zenith direction (3). Measuring the diffuse downwelling irradiance is the same basic procedure as the total downwelling irradiance except the fact that the spectralon is shadowed.

Figure 11: Spectralon mounted on a camera stable tripod with an adjustable unit for the optics pointing downwards to the spectralon for (1) and (2). For the sky radiance measurement in zenith direction the optic device is turned upside down. Location: Meteorological Institute Munich (MIM) at LMU Munich

Measurement concept Aerosol optical depth measurements are usually performed by measuring the direct radiance at discrete wavelengths especially selected to avoid gaseous absorption effects. The key idea of using a spectrometer is in measuring the total downwelling irradiance E_d by capturing the upward radiance reflected by a spectralon. For the field measurements made during the time of the thesis a grey spectralon with 10 % reflectance is used. The spectralon resembles a diffuser exhibiting highly lambertian behaviour. Both the direct sun radiance and the diffuse sky radiance contributes to the total downwelling irradiance. To obtain the diffuse sky radiance the sun is covered by a suitable object fixed at a rod long enough to avoid adjacency

effects. During measurement of the diffuse sky radiance it is important to make sure to cover only the solar disk. Due to Mie scattering the phase function $P(\theta)$ of aerosol is the more directional dependent the bigger the particles are (see Figure (2) in the theory section). Thus covering a larger part of the sun may lead to a covering of a larger part of the diffuse sky radiance resulting in a loss of information considering aerosol parameter like Ångström exponent and turbidity coefficient. The advantage of the measurement of both total downwelling irradiance and diffuse sky irradiance and taking the ratio meaning the reflectance of both spectra is that by dividing both measurements in respect to each other the spectral signature belonging to molecule and aerosol absorption is eliminated. Thus considering radiative transfer models the required set of unknown parameters describing radiance spectra reduces to a smaller set. Moreover disturbing effects like adjacency effects due to local objects are removed as long as it is assured that the geometric measurement setup is not changed between both measurements. If the used spectrometer does not have strong nonlinear behavior with respect to signal intensity one more advantage is that the calculated reflectance is independent of calibration. Thus this might reducing possible errors caused by inaccurate calibration procedures. Additional to the total and diffuse downwelling sky irradiance the measurement of the sky radiance L_{sky} is performed. Thus the optics of the spectrometer are pointed upwards with an zenith angle of 0 °. This is an alternative approach to directly fit the diffuse sky radiance without using a spectralon and to analyze in which way the aerosol information can be retrieved though more variables have to be determined in the inversion process. Moreover adjacency effects of the surroundings or covering problem can be neglected. Since the position of the sun elevation plays an important role for representing the sky radiance model, additionally to each measurement the exact UTC Time stamp and the GPS coordinates are noted.

Models The retrieval of aerosol parameters like Ångström exponent α and turbidity coefficient β is based on the semi-empirical parametrization of the radiative transfer for clear sky conditions based on Bird and Riordan [15] which is presented in the theory section 2.2. To model the irradiance ratio (reflectance) R of the total downwelling and diffuse irradiance E_d (Formula 4) and E_{ds} (Formula 6) the ratio of both components has to be taken. Instead of I referring to the irradiance the model will be represented by the radiance L. In the following the used models reproducing the performed measurements are described:

Irradiance Reflectance :

$$R = \frac{E_{ds}}{E_d} = \frac{L_{ds}\pi}{L_d\pi} = \frac{g_{dsar}L_{dsr} + g_{dsa}L_{dsa}}{\pi\left(L_{dd} + L_{dsr} + L_{dsa}\right)} \tag{44}$$

$$= \frac{1}{\pi} \cdot \frac{g_{dsr}(1 - e^{0.95\tau_r})0.5 + g_{dsa}e^{1.5\tau_r}(1 - e^{\tau_A(\alpha,\beta)})F_a}{(1 - e^{0.95\tau_r})0.5 + e^{1.5\tau_r}(1 - e^{\tau_A(\beta,\alpha)})F_a + e^{\tau_r(\lambda,\theta)+\tau_A(\beta,\alpha)}} \tag{45}$$

The diffuse component arising from multiple ground-air interactions I_g (Formula 9) will be neglected to reduce complexity and it is assumed that the adjacency effects have no significant influence on the aerosol parameter retrieval. The parameters of interests are the Ångström exponent α and turbidity coefficient β. Additionally g_{dsr} and g_{dsa} denoted as **coverty factors** are important factors describing the intensity ratio of irradiance which is not covered. The term g_{dsr} is mainly due to the Rayleigh dependence whereas g_{dsa} refers to the aerosol contribution. During the shadowing parts of the sky radiance are covered which should be included to the

model. It is assumed that due to the same measurement geometry adjacency effects are removed by the division of the spectra.

Sky Radiance :

$$L_{sky} = l_{dsa} I_a(\lambda) + l_{dsr} I_r(\lambda) \tag{46}$$

$$= F_0 cos\theta T_{oz} T_u T_w T_{aa} (l_{dsr}(1 - T_r^{0.95}) \cdot 0.5 + l_{dsa} T_r^{1.5}(1 - T_{as}) F_a) \tag{47}$$

The model to reproduce the sky radiance measurement in the 0 ° direction is given by Formula (6) which thoroughly described in theory section 2.2. This equation contains more unknown parameters which have to be retrieved by the inversion algorithm. In addition to α and β the parameters l_{dsr}, l_{dsa}, H_{oz} (see Formula 21) and wv (see Formula 23) are unknown. Since just a small portion of the diffuse sky radiance is measured the sky radiance equation requires additional factors to adjust for signal intensities received by the detectors. The adjustment is made by the intensity factors l_{dsr} and l_{dsa}. Moreover it has to be considered applying the proposed model that the wavelength dependent absorption coefficients a_{o2}, a_{o3} and a_{wv} of the atmospheric gases like Oxygen, Ozone, and water vapor are independent on temperature and pressure. The absorption coefficients are averaged over the vertical column resulting in a strong simplification of the model. The averaged absorption coefficients with fine resolution were taken from Water Color Simulator 2D WASI4 [16, 51]. The mean extraterrestrial solar irradiance $H_o(\lambda)$ is also taken from WASI4. Averaged absorption coefficients and mean extraterrestrial solar irradiance $H_o(\lambda)$ are shown in Figure 12.

Sky Radiance Irradiance Reflectance :

$$R_{sky} = \frac{L_{sky}}{E_d} = \frac{l_{dsar} L_{dsr} + l_{dsa} L_{dsa}}{\pi \left(g_{dd} L_{dd} + g_{dsr} L_{dsr} + g_{dsa} L_{dsa} \right)} \tag{48}$$

Besides the irradiance reflectance (45) a different approach namely modeling the reflectance ratio of sky radiance L_{sky} and total downwelling irradiance E_d can be performed. In this case the absorption components are also eliminated. In comparison to the irradiance reflectance the equation does have two additional parameters form the sky radiance l_{dsr} and l_{dsa} to determine. They key idea of using this model is to use the retrieved intensity factors l_{dsr} and l_{dsa} from the direct sky radiance measurement as input parameters for this model. The parameter g_{dd} is set to 1. It has to be taken into account that the factors g_{dsr} or g_{dsa} in this model have to be interpreted in a different way then in the irradiance reflectance (45). In this case their relation is not due to shadowing of the sun, but due to different surrounding objects like buildings and measurement setup resulting in values $g_{dsr} < 1$ or $g_{dsa} < 1$. Since the phase function $P(\theta)$ of aerosol particles is not isotrope for θ the assumption holds that $g_{dsr} < g_{dsa} < 1$.

Data processing At each measurement timestamp 30 to 50 measurements are taken. After calibration of these measurements the mean with the standard sample deviation are calculated. By means of Gaussian error propagation the standard deviation of the calculated reflectance is determined. For the model (48) the spectra of the total downwelling irradiance has to be divided by the spectralon reflectance $r_{spectralon}(\lambda)$:

$$E(\lambda) = \frac{E(\lambda)}{r_{spectralon}(\lambda)} \tag{49}$$

The reflectance $r_{spectralon}(\lambda)$ has been measured at Limnological Research Station Iffeldorf (see Figure 13).

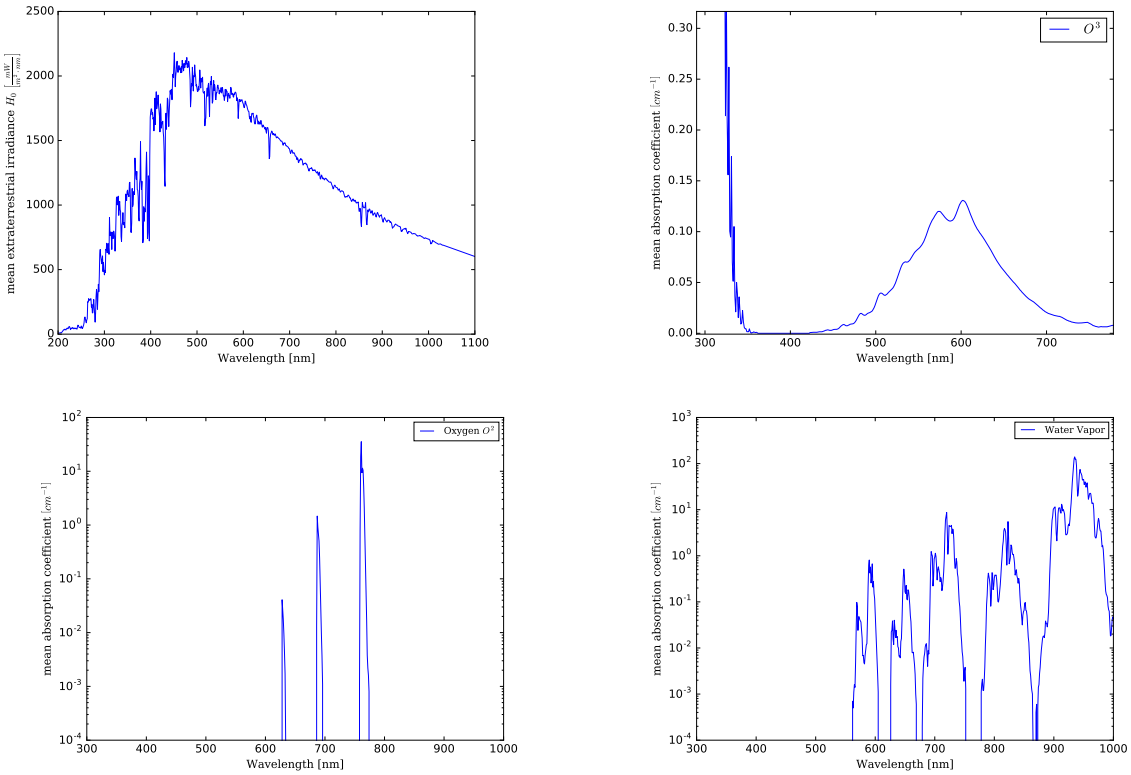

Figure 12: The extraterrestrial and the averaged absorption coefficients of water Vapor, oxygen and ozone are taken from 2D WASI [16, 51]. This was done be inversion of the transmission spectra calculated by MODTRAN (MODerate resolution atmospheric TRANsmission), a software tool for the prediction and analysis of optical measurements through the atmosphere.

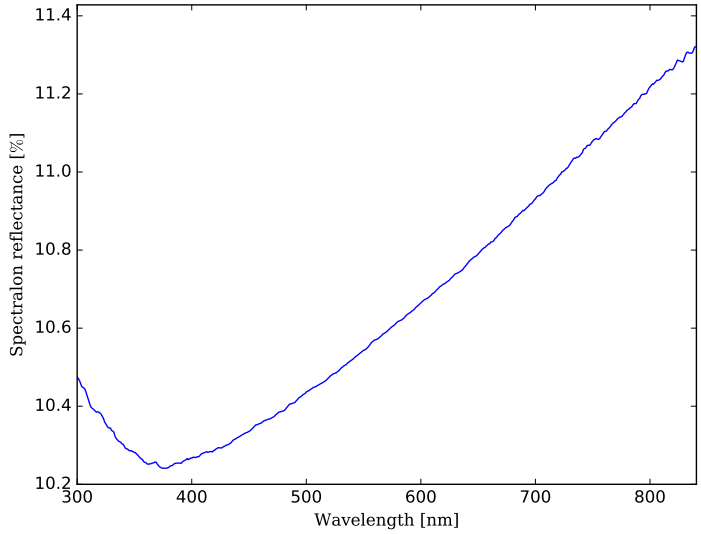

Figure 13: Reflectance of spectralon shows an spectral dependent reflection behavior. Measurement has been performed at imnological Research Station Iffeldorf.

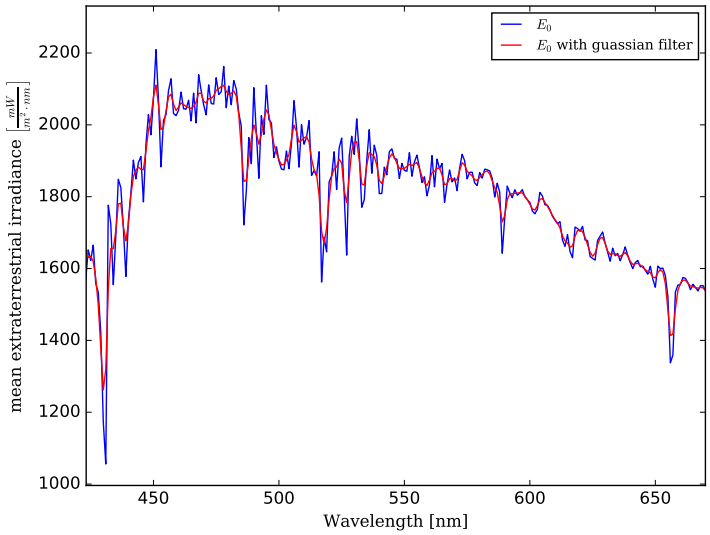

Figure 14: Gaussian filter with the instruments resolution applied to the mean extraterrestrial solar irradiance extracted from WASI4.

Implementation The proposed models are implemented in Python. As input parameters the corresponding UTC Time and GPS location are necessary to calculate the sun zenith angle for air mass (14) and forward scattering probability (15). Weather conditions like relative humidity, pressure and temperature at the time of measurement are automatically downloaded as json packages from a weather station server. The fit of the measured data with the corresponding model to determine the desired parameters are performed by the Python Lmfit package for non-linear least-squares minimization and curve-fitting [52]. Different optimization algorithm like the truncated newton-algorithm, levenberg-marquard, etc. are available and have been tested for the data fitting. The limited-memory Broyden–Fletcher–Goldfarb–Shanno (LBFGS) [53] for bounded-constrained problems belonging to the class of quasi-newton algorithm showed best performance. For a better control a logging was implemented to track the different steps of the parameter retrieval. Via a configuration file parameters for the inversion algorithm could be adjusted easily. An output with the provided fitting information like reduced chi-square are shown in Table 4. The mean extraterrestrial solar irradiance $H_o(\lambda)$ and the averaged absorption coefficients a_{o2}, a_{o3} and a_{wv} have to be adapted to the response of the sensor since the sensor does have an spectral resolution FWHM of ≈ 1.6. Therefore a Gaussian filter corresponding to the sensors resolution is applied to the spectra (see Figure 14).

```
eval - INFO - Tar Date: 2016-11-29 09:39:27
eval - INFO - Ref Date: 2016-11-29 09:38:57
eval - INFO - GPS coords (lat, lon) 48.148 11.573
eval - INFO - Files
   ref: /measurements/LMU/291116_LMU/calibrated/reference003.asc
   tar: /measurements/LMU/291116_LMU/calibrated/target003.asc
 - evaluate_spectra
eval - INFO - E_ds_E_d Ratio
eval - INFO -
   Zenith angle tar 72.096
eval - INFO -
   Zenith angle ref 72.124
eval - INFO -
    Atmospheric path length tar 3.212
eval - INFO -
    Atmospheric path length ref 3.217
eval - INFO -
    Relative humidity 0.746
eval - INFO -
    Pressure 950.847
eval - INFO -
```

```
    Single scattering albedo 0.969
eval - INFO -
    Using lmfit model <<<< FIT
eval - INFO - Using lmfit package
eval - INFO - Method lbfgsb
eval - INFO - Parameter  names ['alpha' 'beta' 'g_dsa' 'g_dsr']
eval - INFO - Setting for alpha: initial: 1.5 and bound [-0.2  5. ]
eval - INFO - Setting for beta: initial: 0.06 and bound [ 0.  5.]
eval - INFO - Setting for g_dsa: initial: 0.5 and bound [ 0.  1.]
eval - INFO - Setting for g_dsr: initial: 0.7 and bound [ 0.  1.]
eval - DEBUG - Setting {} parameters fix
eval - INFO - [[Model]]
[[Fit Statistics]]
    # function evals   = 62
    # data points      = 648
    # variables        = 4
    chi-square         = 611.114
    reduced chi-square = 0.949
[[Variables]]
    alpha:   1.79447733 +/- 0.015843 (0.88%)
    beta:    0.19457588 +/- 0.008372 (4.30%)
    g_dsa:   0.30251912 +/- 0.011991 (3.96%)
    g_dsr:   0.79736234 +/- 0.003711 (0.47%)
[[Correlations]] (unreported correlations are <  0.100)
    C(beta, g_dsa)               = -0.996
    C(beta, g_dsr)               = -0.925
    C(g_dsa, g_dsr)              =  0.889
    C(alpha, g_dsa)              =  0.482
    C(alpha, beta)               = -0.409

 - evaluate_spectra
eval - INFO - Convergence: True
```

Table 4: Logging output of performed parameter retrieval on each average. The UTC Time and the GPS coordinates serve as input parameters for the corresponding model calculation. Bounds and initial values and fit results from lmfit package are shown.

3.3.2 Microtops sunphotometer

Aerosol optical thickness and micro physical aerosol properties can be deduced from the investigation of the solar light scattered and attenuated by the atmosphere by ground-based remotes sensing techniques. The direct sun measurements of sun photometers involves the measurement of the transmitted attenuated direct solar beam at each channel. The physical theory is based on the Beer-Bogour (Formula 28).

$$V_\lambda = \frac{V_{0\lambda}}{R^2} e^{-\tau_{total} M} \tag{50}$$

with

V_λ: measured signal at the wavelength λ

$V_{0\lambda}$: a the extraterrestrial signal constant referenced to the mean Earth Sun distance at wavelength λ

R: Earth Sun distance correction in Astronomical units at time of measurement

τ_{total} total optical thickness

M: Optical air mass

To retrieve the aerosol optical thickness τ_a from the measured optical thickness τ one has to subtract Rayleigh scattering and absorption processes by other atmospheric constituents like water Vapor, ozone O_3 and other gaseous pollutants (e.g. NO_2, CO_2, CH_4) [54, 55].

$$\tau_a(\lambda) = \tau_{total}(\lambda) - \tau_{wv}(\lambda) - \tau_r(\lambda) - \tau_{o_3}(\lambda) - \tau_{gas.abs.}(\lambda) \tag{51}$$

Consequently the received signal handled by Microtops II sun photometer writes:

$$V(\lambda) = \frac{V_0(\lambda)}{R^2} e^{(-m(\theta)\frac{p}{p_o}\tau_r(\lambda) - m_{o_3}(\theta)(\tau_{o_3}(\lambda) - \tau_{N0_2}(\lambda)) - m(\theta)\tau_a(\lambda))} \tag{52}$$

One usually selects channels less effected by gaseous absorption. Microtops II derives the aerosol optical thickness by five discrete channel with wavelength 380 nm, 440 nm, 500 nm, 675 nm and 870 nm. Since the channel 940 nm serves as suitable signal information for the water vapor channel it is not included into the AOD calculation. So it can be removed for the further analysis:

$$\tau_a = \frac{1}{m(\theta)}(ln\frac{V_0(\lambda)}{V(\lambda)R^2} - m(\theta)\frac{p}{p_0}\tau_r(\lambda) - m_{o_3}(\theta)(\tau_{o_3}(\lambda) - \tau_{N0_2}(\lambda)) \tag{53}$$

with the ozone path:

$$m_{o_3} = \frac{1}{1 - v^2 sin(\theta)^2} \quad \text{with} \quad v = \frac{(R+r)^2}{(R+h)^2}, \quad h = 26 - 0.1 \cdot Lat[^\circ] \tag{54}$$

$$\tau_r(\lambda) = 0.00864 \cdot \lambda^{-(3.916 + 0.074\lambda + \frac{0.050}{\lambda})} \cdot \frac{p}{1013.5} \tag{55}$$

$$\tau_{O_3}(\lambda) = a_{O_3}(\lambda) \cdot O_3 \cdot m_{O_3} \tag{56}$$

The calculation of Rayleigh optical depth is straightforward. The air pressure p during measurement time is provided by Microtops Sunphotometer. The extraterrestrial constant $lnV_0(\lambda)$ and ozone absorption coefficient a_{O_3} are known as calibration constants. The airmass $m(\theta)$ is calculated by Formula (14) . The Ångström exponent (see Formula 30) represents the negative slope of AOT with wavelength in logarithmic scale. Using at least two wavelengths (channels) this parameter can be calculated by means of least squares methods as presented in Formula (31).

$$\alpha = -\frac{dln(\tau_a)}{dln(\lambda)} \tag{57}$$

The turbidity coefficien β with respect to 550 nm is the intersection of y-axis. An calculation example is shown in Figure 15. Considering the extinction measurement of the total optical thickness τ the scattered light entering the instrument has to be corrected for to ensure that the measured signal is due to extinction alone. For a more detailed description the reference [13] is recommended.

3.3.3 AERONET Cimel Sunphotometer

Besides the spectral AOT the measurement of sky radiance over a large range of scattering angles from the sun AERONET uses sophisticated algorithms for the micro physical properties retrieval of aerosols. The determination of aerosol properties from light scattering and extinction radiance measurements are described as inversion problems. In comparison to Microtops II AERONET performs besides direct sun measurement the sky radiance measurement in four spectra bands 440, 670, 870, 1020 nm. AERONET provides three different quality levels for data download. Quality Level 1.0 is marked as unscreened while Level 1.5 is marked as cloud-screend meaning data quality checks like stability and smoothness criterions have been applied to remove possible outliers. Both levels are available at real-time. A further description considering to cloud screening procedure can be found in [56]. Level 2.0 data products are available after 12 months or longer and ensure the highest quality data accounting for e.g. instrumental performance check and sensor temperature stability checks. For the inversion algorithms several presumptions are made:

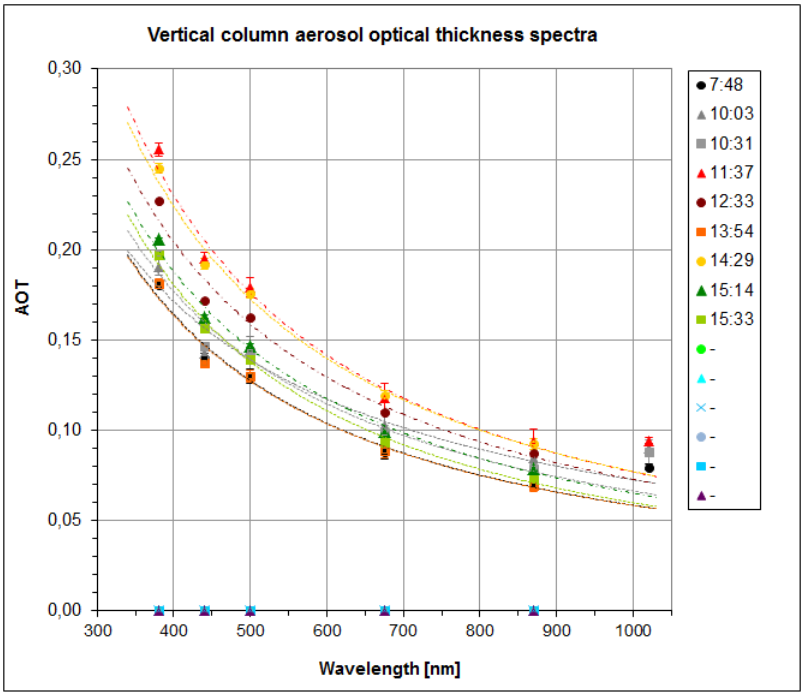

Figure 15: Microtops evaluation. A regression fit is performed to retrieve the Ångström exponent α and turbidity coefficient β. On the x-axis the corresponding discrete channels of Microtops II are plotted. On the y-axis the calculated aerosol optical thickness can be seen calculated with Formula (53). This is an example date of the 13th September on the roof of DLR (Oberpaffenhofen). Excel program developed by Bringfried Pflug. (an peter und sebastian REFERENCE?)

- Two sets of aerosol particles: spherical shapes and spheroidal shapes (complex index of refraction is same)
- Plane parallel atmosphere
- Homogeneous vertical distribution of aerosols in the almucantar inversion
- BRDF reflectance of the ground surface
- Assumption of uncorrelated log-normally distributed errors

Thus inversion algorithm retrieval provides aerosol size distribution and complex refractive index based on spectral aerosol optical thickness measurements and on the angular distribution of the sky radiance (see Formula 32). Scattering on homogeneous Mie-spheres are implemented in the inversion algorithm for the aerosol microstructure.

$$L(\theta, \lambda) = L(n(r), m(r)) \tag{58}$$

Based on this the phase function $P(\theta)$, the partition of spherical/non-spherical particles, the single scattering albedo ω_0 are retrieved [57] . A more detailed description of how to retrieve the phase function by a large range of scattering angles is provided in [58]. For AERONET stations the inversion algorithm from Dubovik and King [59] based on the analysis of the intensity of scattered light is used to retrieve simultaneously particle size distribution and complex refractive index.
The turbidity coefficient is not provides by AERONET data download. For this thesis the Ångström formula (30) with the retrieved Ångström parameter is used to determine the turbidity coefficient β via fitting.

Error assumption It can be shown that the particle size distribution can be retrieved below an error of approximately 25% and the aerosol optical depth τ_a can be determined with an accuracy of $\Delta\tau_a < 0.01$ for long wavelengths and $\Delta\tau_a < 0.02$ and the standard deviation of error in sky radiance measurements is assumed to be below 5% [60].

3.4 Sensitivity Analysis

Before solving the inverse problem for the analytic radiative transfer equation the information content of corresponding measurements with respect to the required parameters has to be checked. To determine the accuracy of extracting aerosol parameters by means of inversion algorithms of the three different models a sensitivity analysis is performed. It aims to describe how much the output values of the inversion algorithms are affected by changes in model input values. This provides a detailed information addressing the relative significance of errors in different parameters. There exists various techniques to determine how sensitive inversion outputs are to changes in model inputs. The main idea is to vary one or a set of parameter values at a time and look at the change of the desired output values. For models like the Sky Radiance L_{sky} containing more than four unknown atmospheric parameters it can be analyzed if setting specific parameters to a fixed value would result in significant biases of the variable of interest. The sensitivity analysis substantially follows the approach presented by Gege (2008) [61].

Method At first parameters p represent the correct model parameters to generate simulation data $L(p)$ reproducing real-scenario downwelling irradiances. Gaussian noise equal to the sensor noise is added to the simulation data $y = L(p) + Noise$. Depending on the desired parameters of interest a set of parameters p_f is chosen which are fix during inversion processing. A bias offset Δp_f is added to the fixed parameters $\tilde{p_f} = p_f + \Delta p_f$. The rest of parameters, variables, are marked as p_v. During inversion via fitting the biased fixed parameters $\tilde{p_f}$ stay fix while the optimized parameters are retrieved p'_v to best fit the simulation data. In this way the resulting parameters p'_v do not equal the simulation parameters p_v but are biased with and error $p'_v = p_v + \Delta p_v$ caused by $\tilde{p_f}$. To obtain statistical information the inversion method runs N times adding noise on the simulation data. Then the mean value $\tilde{p}'_v$ of all p'_v is calculated. This provides information about in which way these parameters are correlated and in how strong they are affected by different parameters. A detailed scheme of this procedure is shown in the diagram 16.

For the final result relative error for the extracted parameters is calculated as:

$$\Delta p_v = \frac{\tilde{p}'_v - p_v}{p_v} \cdot 100 \tag{59}$$

Models and parameters The used models with the corresponding fitting variables for the sensitivity analysis are the sky radiance L_{sky}, the ratio of diffuse and total downwelling irradiance $\frac{E_{ds}}{E_d}$ and the ratio of the sky radiance and downwelling irradiance $\frac{L_{sky}}{E_d}$. The corresponding parameters describing the models are listed in Table 5.

Table 5: Models and parameters analyzed with a sensitivity analysis.

Model	Parameters
Sky Radiance L_{sky}	wv, H_{oz}, l_{dsr}, l_{dsa}, α, β
Irradiance Ratio $\frac{E_{ds}}{E_d}$	g_{dsr}, g_{dsa}, α, β
Sky Radiance Irradiance ratio $\frac{L_{sky}}{E_d}$	l_{dsr}, l_{dsa}, g_{dsr}, g_{dsa}, α, β

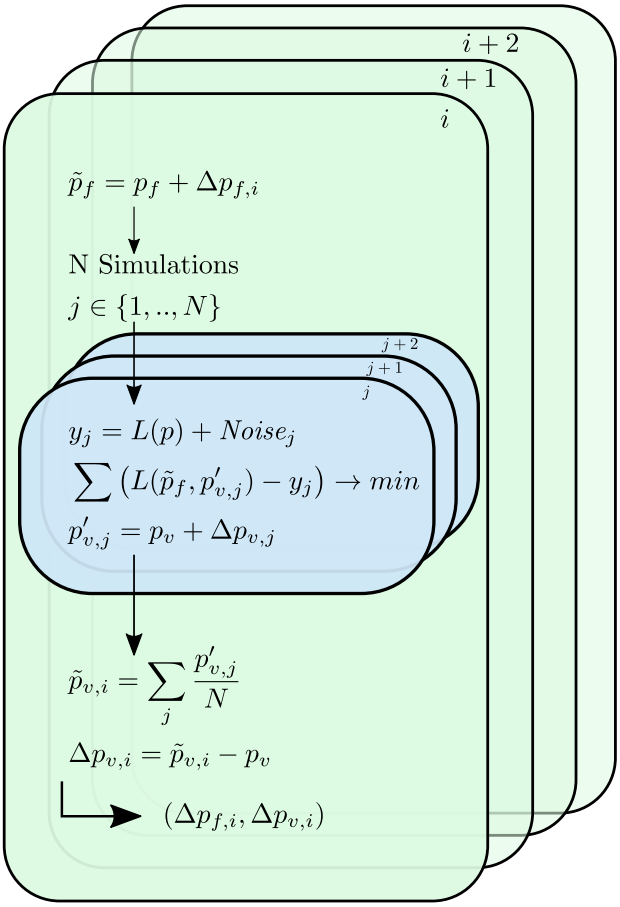

Figure 16: Implementation of the sensitivity analysis:
The variable p is the set of all parameters describing the model. This set is separated into parameters p_f which are hold constant (fixed) during inversion and p_v which are variable. The implementation consists of an inner and outer loop. In the outer loop predefined Δp_f are added to the exact value. For obtaining statistical information several iterations generate noisy signal used as reference for the least squares minimization. The mean value of the parameters $p'_{v,j}$ is calculated and subtracted from the true value p_v.

4 Results

4.1 Laboratory Results

The spectrometer characterization is done by means of a stable calibrated reference light source. For this the RASTA (RAdiation STAndard) at the CHB Laboratory is used. The reference light source is a tungsten-halogen lamp (Gamma Scientific Model 5000-16C) widely used as irradiance standard. As described in the methods section the integration time of the spectrometer is monotonically increased while the light source intensity is kept constant. This is done starting with the integration time 5 [ms] to 120 [ms]. The tungsten-halogen lamp shows a spectral radiance with higher intensities in the range 500 [nm] to 800 [nm]. Along with each radiance measurement a darkcurrent measurement is made. The results are shown in Figure 17.

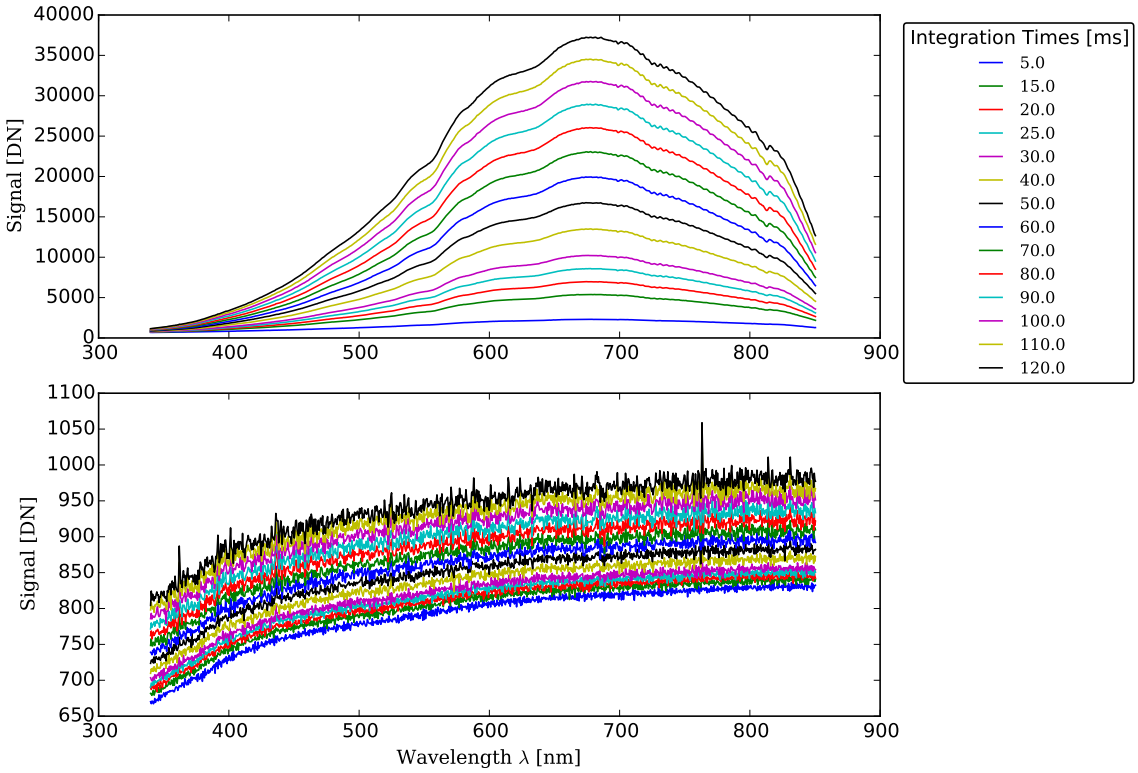

Figure 17: Measurements taken at the RASTA with a tungsten-halogen lamp as calibrated light source. The upper picture shows the measured radiance signal [DN] with increased integration time in steps of 5 or 10 [ms]. Along with these measurement the darkcurrent signal [DN] was measured.

Nonlinearity characterization The goal is to generate characterization data as the nonlinearity corrections function $\gamma(\lambda)$. As discussed in the previous section the nonlinearity of the CCD detector has to be corrected for. The offset gain of the A/D Converter which is added to the CCD signal is not known in advance. Therefore for each channel the signal is plotted versus the measured integrations time (see Figure 18). To suppress thermal darkcurrent noise which does show nonlinear behavior the signal is extrapolated with a linear function to the integration time zero. The extrapolated signal is assumed to be the pure offset gain of the measured. The ibsen spectrometer lacks an internal temperature stabilization to reduce thermal noise. Thus ambient temperature has to be taken into account during experimental measurements. Two

darkcurrent measurements were made at an ambient temperature of $30°C$ in summer and at $-3°C$ in winter which are shown in Figure 19. In comparison to the darkcurrent signal at an ambient temperature at $-3°C$ the temperature increase of about $30°C$ leads to a increase of the thermal noise by approximately $\approx 40\%$. For further investigation the extrapolated offset signal S_{off} and the measured darkcurrent signal S_{dark} will be distinguished during nonlinearity correction.

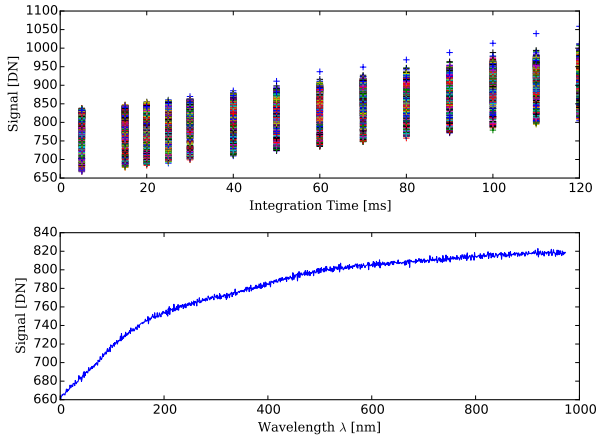

Figure 18: The offset signal [DN] has to be subtracted from the measured signal [DN]. To get rid of the thermal noise each channel with the corresoning integration time signal is extrapolated to signal with integration time 0 (upper image). Thus the deduced offset signal can be shown in the lower figure.

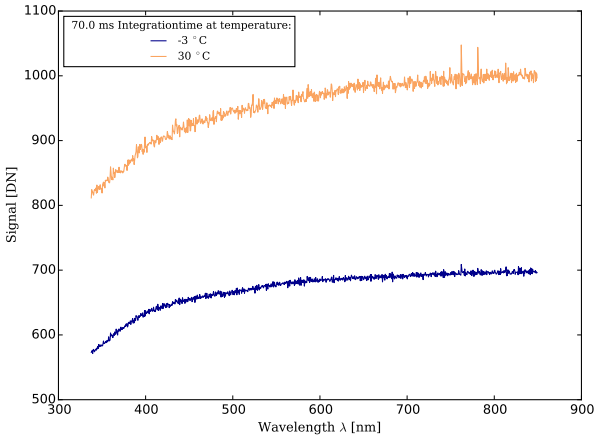

Figure 19: The CCD Detector of the Ibsen spectrometer lacks an active temperature stabilization. As a consequence different temperature conditions have impact on the darkcurrent signal making the gain offset extraction more difficult. For extreme temperature differences like $30°C$ the darkcurrent rises by $\approx 40\%$. It is important that for each measurement of the radiance the corresponding darkcurrent measurement is made.

For the nonlinear characterization for both the extrapolated offset signal S_{off} and the measured darkcurrent signal S_{dark} are subtracted. Then the nonlinear characterization procedure is applied on both preprocessing steps. The results on the applied spectra normalized to one [ms] are shown in Figure 20. It should be reminded that the assumption holds that the nonlinear behavior is the same for all channels of the CCD sensor.

$$\Delta\% = \sigma(S_i)/S_i \cdot 100 \quad \text{with} \quad i = ith\ Channel \tag{60}$$

The nonlinearity correction works both the darkcurrent S_{dark} and offset signal S_{off} corrected signal reducing the error from 4% to below 1%. The tungsten-halogen lamp shows low radiance intensities in the low wavelength regime $[350 - 500$ nm$]$. Thus the correction of the nonlinearity in this regime is lost in the noise. A second stable light source at the CHB is set up to validate the nonlinear correction functions. Radiances with increasing integration times were measured. The nonlinear correction function was applied to each measurement and then normalized to one millisecond (see Figure 21). The standard deviation error can be reduced from 2.5% to 1.0% for both S_{dark} and offset signal S_{off} corrected signal. As mentioned before the spectrometer does not inhibit an active thermal stabilization. Experimental in situ measurements are performed at different weather conditions. The subtraction of the calculated offset gain could lead to biases in the nonlinearity correction since the thermal noise increases. The nonlinear correction function $\gamma(S)$ is shown in Figure 22. Referring to Figure 19 the increasing signal of about $\approx 40\%$ results

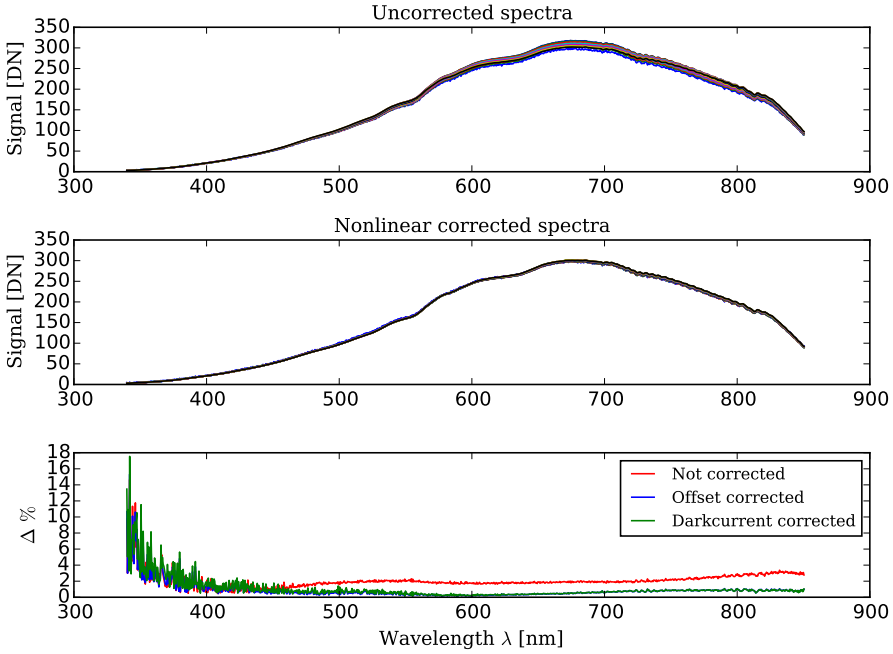

Figure 20: The normalized raw signals of the RASTA show a nonlinear behavior in respect to different intensities falling on the CCD sensor. If the CCD sensor operates linear the normalized spectra should be superimposed. The measured signal is divided by $\gamma(S)$ for nonlinear correction. Both the darkcurrent S_{dark} and offset signal S_{off} corrected signal are corrected. The nonlinearity correction works both the darkcurrent S_{dark} and offset signal S_{off} corrected signal reducing the error from 4% to below 1%.

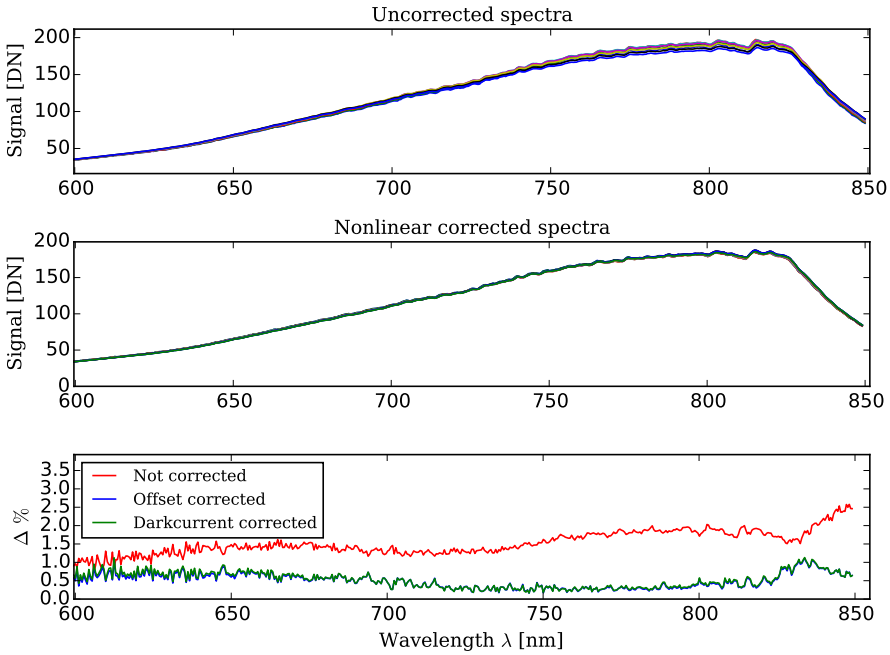

Figure 21: A second calibration setup with a stable lamp was built up to test the correction function $\gamma(S)$. Similar to Figure 20 the nonlinearity correction works both the darkcurrent S_{dark} and offset signal S_{off} corrected signal reducing the error from 4% to below 1%.

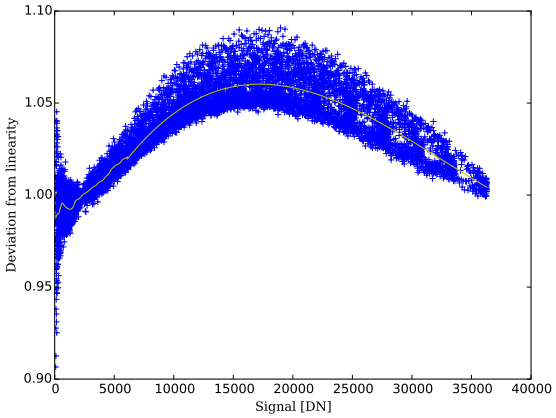

Figure 22: The nonlinear correction function $\gamma(S)$ fitted to the data by a cubic spline function. The nonlinear correction function is applied to the corresponding signal intensity [DN].

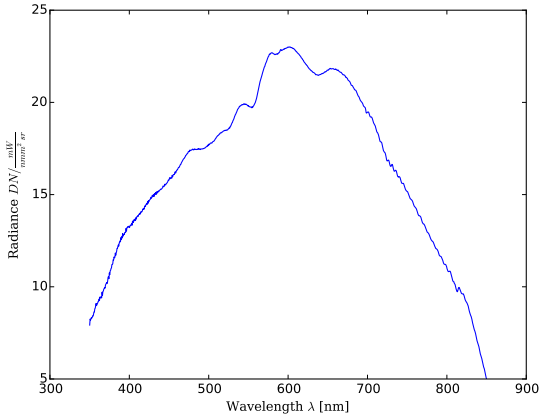

Figure 23: The response factor $r(\lambda)$ to convert the signal from [DN] into the corresponding phyiscal unit $\left[\frac{mW}{m^2nm \cdot sr}\right]$. The etalon effect in the near infrared regime can be clearly seen.

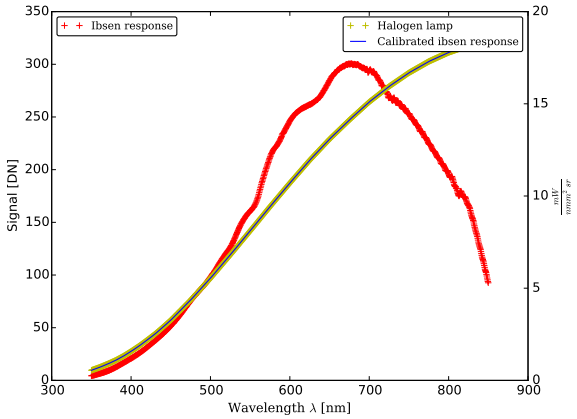

Figure 24: This Figure shows the calibration of the raw Ibsen response. This signal refers to the left side of the y-Axis in [DN]. The calibrated signal and the reference halogen light bulb values are referring to the right side of the y-Axis in the radiance L units $\left[\frac{mW}{m^2nm \cdot sr}\right]$

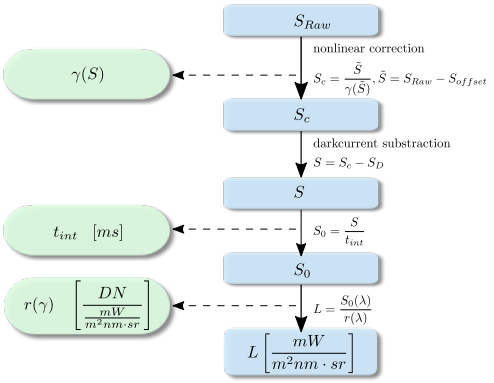

Figure 25: (an sebastian und peter: Das bild wird noch bearbeitet

in an estimated error in respect to $\gamma(S)$ of less than $\approx 1\%$ if the measured signal is around 34000 [DN] (see Figure 22). The nonlinearity correction function of the darkcurrent subtracted signal results in a the correction up to 2% and is more reasonable referring to increasing thermal noise at high ambient temperatures whose nonlinearity cannot be traced back to its electronic origin.

Radiometric characterization The resonse factors $r(\lambda)$ to map the measured digital signal in [DN] to the correct physical unit $\left[\frac{mW}{m^2nm \cdot sr}\right]$ of the radiance L (see Figure 23.) The factors were calculated by formula (43). The etalon effect causing modular intensity signal through back-and-forth reflection in the depletion region and creating interferences is clearly visible for the near infrared regime. For validation of the calibration the calibrated spectrometer signal, the reference intensity of the tungsten-halogen light of RASTA and the raw Ibsen signal are shown

in Figure 24

Error discussion The lack of active temperature stabilization introduces uncertainties in the Level 1 calibration procedure considering variable experimental surrounding conditions as different ambient temperatures. By cooling the thermally generated darkcurrent signal of the CCD sensor would be minimized and result in an more reliable calibration processing. Moreover temperature variations have an influence of the refractive index of the active region and thus the etalon effects are temperature dependent. Since the radiometric characterization is performed at laboratory temperature this results in additional errors in the radiometric calibration at different ambient temperatures which currently cannot be estimated.

For the Level One processing the generated characterization files are used. To each radiance signal the corresponding darkcurrent signal file is measured. A calibration scheme is shown in Figure 25.

4.2 Simulation Results

Before analyzing experimental results the derived models for the atmospheric radiative transfer are checked on accuracy and thus reliability of its output. As described in section 3.4 a sensitivity analysis is applied on the irradiance reflectance, the sky radiance and the sky radiance ratio to determine which parameters can be extracted reliable or which parameters should be interpreted with caution. In the following section the results are shown for all three models.

4.2.1 Irradiance Reflectance

For the irradiance reflectance simulation a proposed empirical parameter set resembling real data produced by clear blue sky conditions are chosen. The chosen parameter for the forward calculation are presented Table 6.

Model $\theta = 76\,^\circ$	Parameters
Irradiance Reflectance $\frac{E_{ds}}{E_d}$	$g_{dsr} = 0.8$, $g_{dsa} = 0.5$, $\alpha = 1.8$, $\beta = 0.06$

Table 6: Foward modelling

A sensitivity analysis is performed by varying the coverty factors g_{dsa} and g_{dsr} over an determined range $\Delta g \approx -40\%$ to 40%. This results in an bias in the Ångström exponent $\alpha + \Delta\alpha$ and the turbidity coefficient $\beta + \Delta\beta$ which are presented in Figure 26 and 27. The relative error for the Ångström exponent α is calculated as:

$$\Delta\alpha\,[\%] = \frac{\alpha_{fit} - \alpha}{\alpha} \cdot 100 \tag{61}$$

The minus in front of the per cent symbol originates from the negative difference between desired and fitted parameters. For the turbidity coefficient β the absolute error $\Delta\beta = \beta_{fit} - \beta$ is more representative and therefore used as result in Figure 27. It can be easily seen that the Ångström exponent α is insensitive to the variation of the coverty factor g_{dsa} depending on both Rayleigh and aerosol contribution. An error of 60 % does have a small influence on the retrieval of α but an error of g_{dsr} of below 10 % causes a parameter error between 10 to 30 %. Consequently a-priori estimations for g_{dsa} have a smaller impact on the retrieval of the Ångström parameter than g_{dsr}. This means that as long as the coverty factor g_{dsr} cannot be determined reliably the parameter has to remain unknown and be used as fit parameter for the inversion algorithm. The picture is somewhat different for the turbidity coefficient β. Figure 27 does show a strong dependency on both coverty factors. Meaning setting g_{dsa} to fix a-priori estimation would not have significant impact on α but the turbidity coefficient cannot be retrieved reliably. To further analyse this correlation, only one parameter g_{dsa} is varied and the other parameters are fitted. The results are shown in Figure 28. The y-axis shows the relative error in per cent for all fitting variables. An error of 20 % causes an error of below 4 % for g_{dsr} and α but an relative error of $\approx 20\%$ of β. Looking at Figure 29 the variation of g_{dsr} shows a strong correlation between the turbidity coefficient β and g_{dsa}. From the picture it can be concluded that the parameters β and g_{dsa} cannot be separately identified and that considering experimental measurements the retrieval of the turbidity coefficient is challenging. On the basis of the problems identified it is obvious that the ambiguity of the turbidity coefficient cannot be retrieved from the irradiance reflectance alone. An approach is elaborated to determine the desired parameters by the combination of sky radiance model L_{sky} and the sky radiance total downwelling irradiance ratio $R_{sky} = \frac{L_{sky}}{E_d}$.

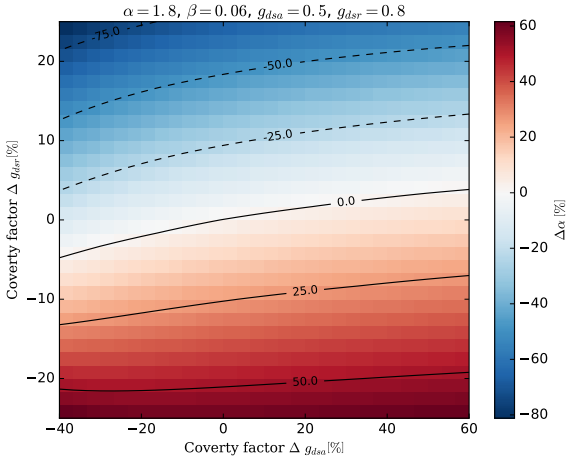

Figure 26: 2D Sensitivity analysis of the irradiance reflectance model $\frac{E_{ds}}{E_d}$. Varying the coverty factor g_{dsa} does not have any significant influence on the retrieval of the Ångström exponent α. Thus a not exact a-priori estimation would still guarantue results in the error range of below 5 %. The parameter g_{dsr} is treated as treated as fitting variable.

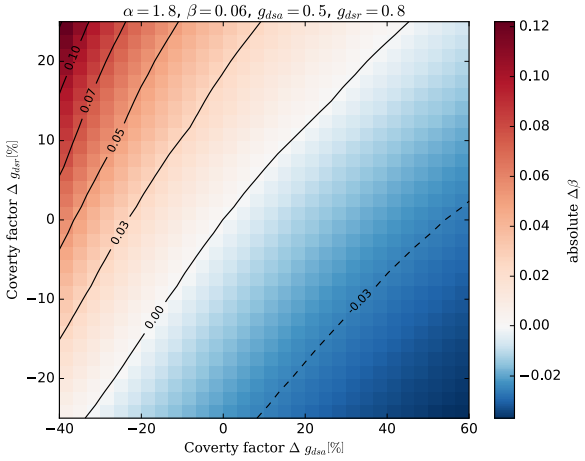

Figure 27: 2D Sensitivity analysis of the irradiance reflectance model $\frac{E_{ds}}{E_d}$. The turbidity coefficient β shows strong correlation to both coverty factors and hence cannot be deduced independently. Considering the model fitting the results should be treated and interpreted carefully.

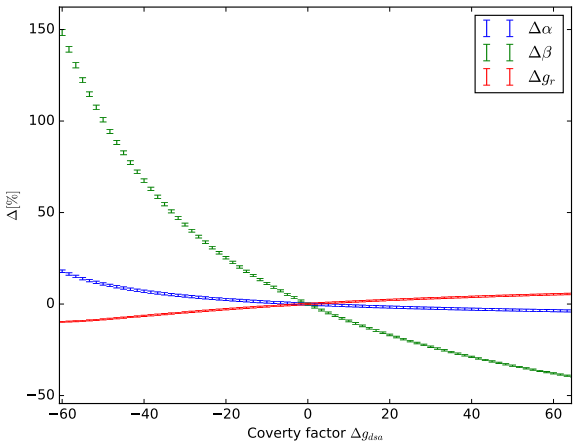

Figure 28: Sensitivity analysis of the irradiance reflectance model $\frac{E_{ds}}{E_d}$. The parameter g_{dsa} is varied over broad range resulting in a strong bias in the turbidity coefficient β.

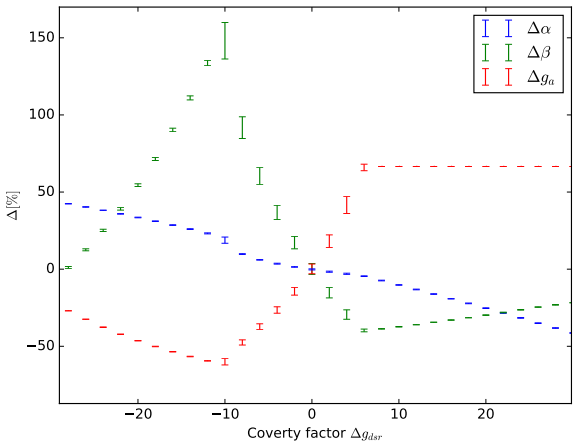

Figure 29: Sensitivity analysis of the irradiance reflectance model $\frac{E_{ds}}{E_d}$. Varying g_{dsr} it is obvious that β and g_{dsa} compensates each other. For experimental data sets problems occur to resolve this ambiguity.

4.2.2 Sky Radiance

Besides the Ångström exponent α and the turbidity coefficient β the sky radiance model L_{sky} contains the intensity factors l_{dsr}, l_{dsa} the ozone scale height H_{oz} $[cm]$ and Water Vapor wv $[cm]$. The intensity factors are important factors to determine intensity contributing to Rayleigh scattering and aerosol scattering. The first step is to analyze the variations of the desired parameter at different spectral regimes. Reminding Figure 12 the influence of the ozone scale height and the water vapor are obviously limited at spectral regimes. The variation of the intensity factors can be analyzed by e.g a analyzing the derivative or running forward model computations with defined values. For the sky radiance simulation a sun zenith angle of 76 ° is chosen since the experimental measurements were taken at higher zenith angles.

Model $\theta = 76\,^\circ$	Parameters
Sky Radiance L_{sky}	$wv = 1.2[cm]$, $H_{oz} = 0.34[cm]$, $l_{dsr} = 0.17$, $l_{dsa} = 0.1$, $\alpha = 1.8$, $\beta = 0.06$

Table 7: Foward modelling

The results are shown in Figure 30. Due to the Rayleigh l_{dsr} shows the highest variability at shorter wavelengths. Thus determining l_{dsr} in this regime results in a a-priori estimation for the intensity factor. Considering β and l_{dsa} a separation of these parameters by inversion modelling is challenging. The form of variation considering Ångström exponent α describes a expected but not strong twist at $\lambda = 550nm$ (see Formula 30).

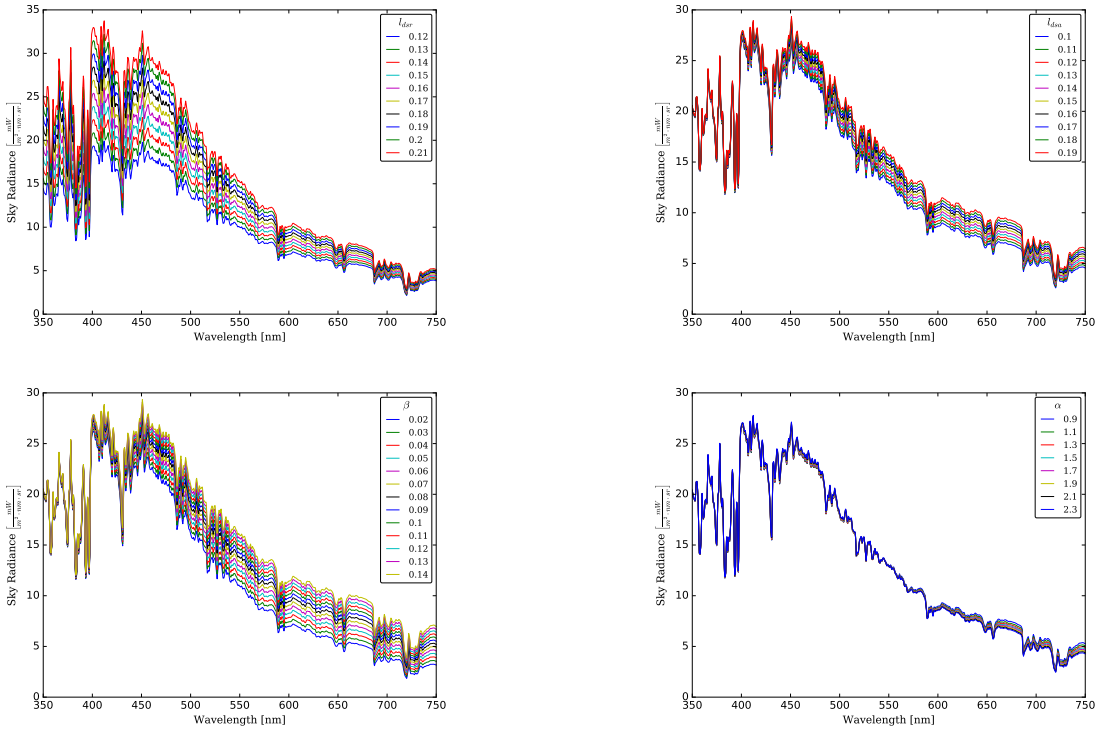

Figure 30: Forward model computation with variation of parameters l_{dsr}, l_{dsa}, β, and α. The ozone height scale is set to $H_{oz} = 0.34[cm]$, water vapor to $wv = 1.2[cm]$, Ångström exponent $\alpha = 1.8$, turbidity coefficient $\beta = 0.06$, $l_{dsr} = 0.17$ and $l_{dsa} = 0.1$.

The parameter l_{dsr} can be retrieved with an accuracy below 1 % keeping H_{oz} and wv constant

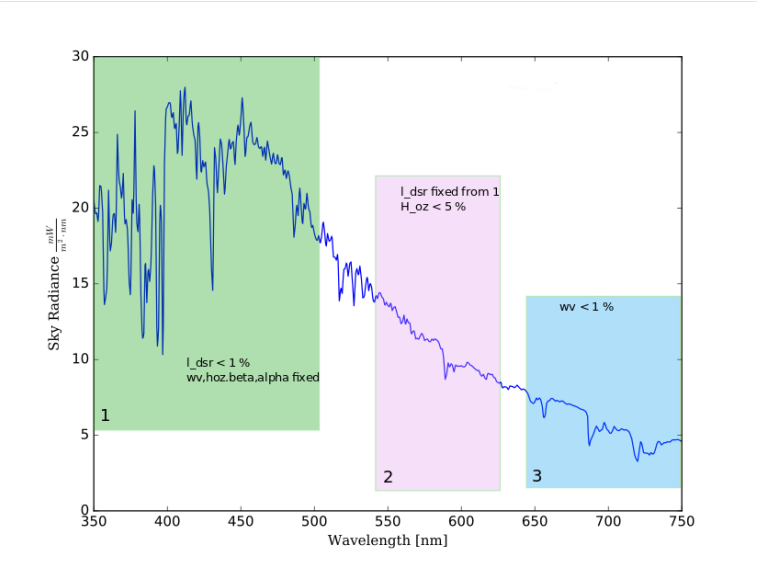

Figure 31: Forward model computation with variation of parameters l_{dsr}, l_{dsa}, β, and α. The ozone height scale is set to $H_{oz} = 0.34[cm]$, water vapor to $wv = 1.2[cm]$, Ångström exponent $\alpha = 1.8$, turbidity coefficient$\beta = 0.06$, $l_{dsr} = 0.17$ and $l_{dsa} = 0.1$.

at a wavelength range of 350 to 400 nm (Figure 32a). With the irradiance ratio a retrieval of the Ångström exponent α gives reliable results. This parameter can serve as an input for the sky radiance model. In Figure 32b he expected invariance in respective to β are demonstrated. It can be seen that the variation of β in the wavelength regime has no influence on l_{dsr}. By holding H_{oz} and wv fix and varying α and β the results promise a retrieval below 1 % even if α has an error of 30 %. The intensity factor l_{dsr} can serve as an input parameter of next retrieval iterations like water vapor and ozone scale height. Thus l_{dsr} is hold fixed during inversion processing. It can be shown that water vapour due to its spectral properties is easily determined with an accuracy below 1 %. It has to be taken into account that problems may occur if adjacency effects in the NIR regime have an impact on the measurements. Vegetation reflectance in the near infrared regime 680 and 750 nm have an rapid change between 5-50 % (Red Edge). The ozone scale height is clearly dependent of the former retrieval of α by the irradiance ratio model. Assuming a Ångström exponent α result with an accuracy below 30 % the ozone scale height can be determined with a 5 % accuracy range. Hereby a fitting range of 540 to 640 nm is chosen. The results and the spectral regions are shown in 47. Finally investigating the full wavelength range of the spectrometer the Ångström exponent can be determined below 10 % account for errors in the prior retrieved parameters. The turbidity coefficient is highly sensitive l_{dsa}. Consequently it is not possible to derive both values l_{dsa} and β simultaneously from the sky radiance measurements.

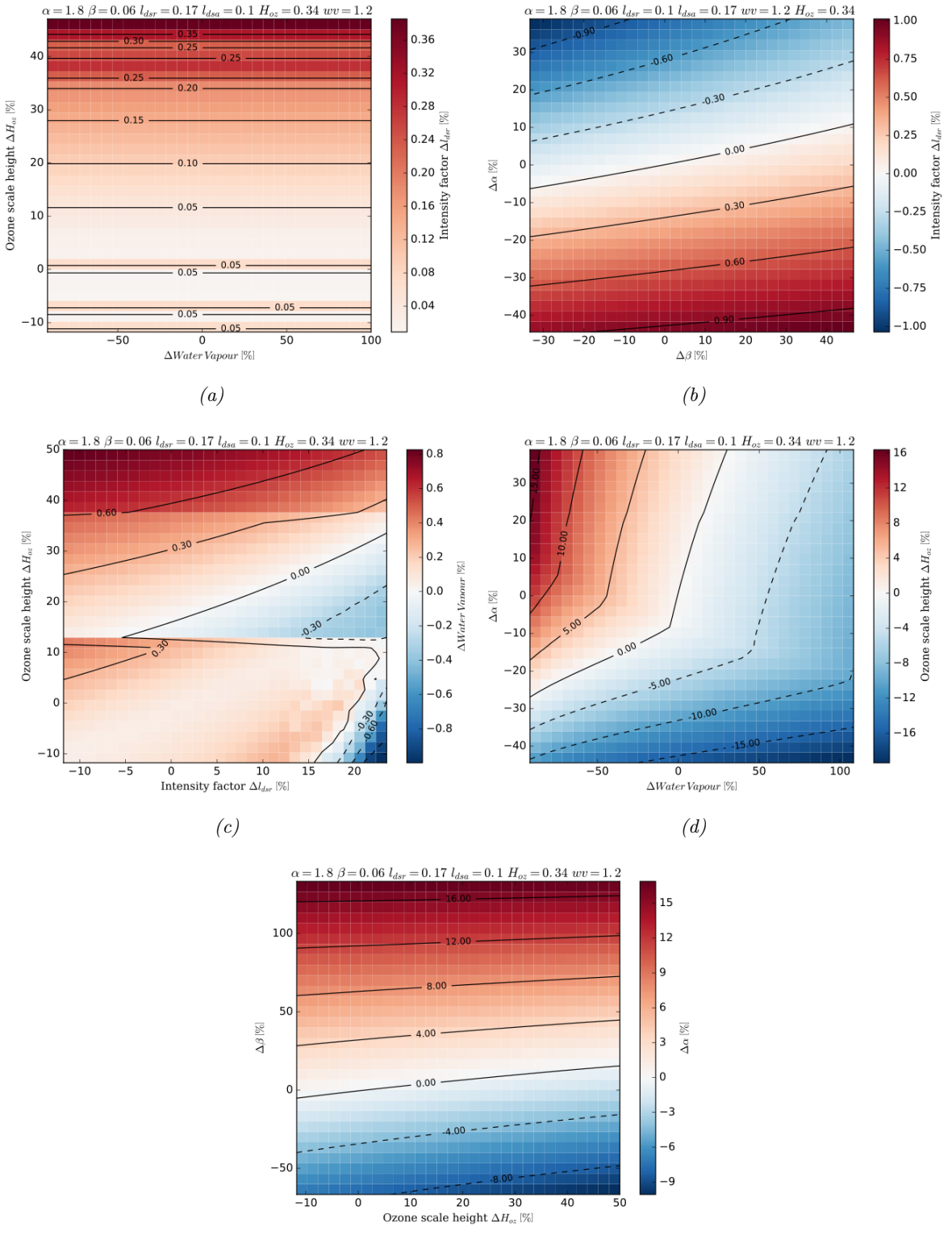

Figure 32: (a)Biased H_{oz} and wv do have no impact on retrieval of the intensity factor . Fitting range: [300nm-450nm]. (b) H_{oz} and wv are hold constant. Depending on a-priori α the retrieval of l_{dsr} is reliable. Fitting range: [300nm-450nm]. (c) Assuming a Angstrom exponent α result with an accuracy below 30 % the ozone scale height can be determined in a 5 % accuracy range. l_dsr is constant. Fitting range: [540nm-640nm].(d)Water vapour wv is determined with an accuracy below 1 %. Problems may occur if adjacency effects in the NIR regime have an impact on the measurements. Fitting range: [650nm-750nm] (e)

4.2.3 Sky Radiance Ratio

Taking the Ångström parameter and the l_{dsr} of prior measurements the turbidity coefficients β can be derived by the sky radiance diffuse irradiance reflectance. For the forward modelling the parameters are similar like in the previous section and listed in Table 8. It is shown that β is insensitive to a variation of g_{dsa} (see Figure 34). Thus it is reasonable to set g_{dsa} to a specific value. Since the most light intensity due to aerosol scattering originates from around the sun this value is chosen slightly below 1. For clear sky conditions the retrieval of the turbidity turns out to be challenging. Assuming a good retrieval of l_{dsr} by means of the sky radiance L_{sky} below an accuracy of 2 % and an Ångström exponent α below an accuracy of 15 % results in an accuracy of $\approx 30\%$ of the turbidity coefficient.

Model $\theta = 76\,^\circ$	Parameters
Sky Radiance $\frac{L_{sky}}{E_d}$	$g_{dsa} = 0.8$, $g_{dsr} = 0.9\, l_{dsr} = 0.17$, $l_{dsa} = 0.1$, $\alpha = 1.8$, $\beta = 0.06$

Table 8: Foward modelling

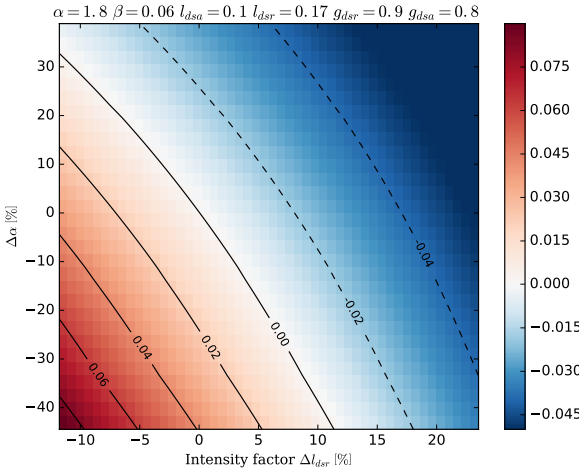

Figure 33: The turbidity coefficient β is dependent of the adequate a-priori estimations of α and l_{dsr}. An accuracy below 30 % is possible.

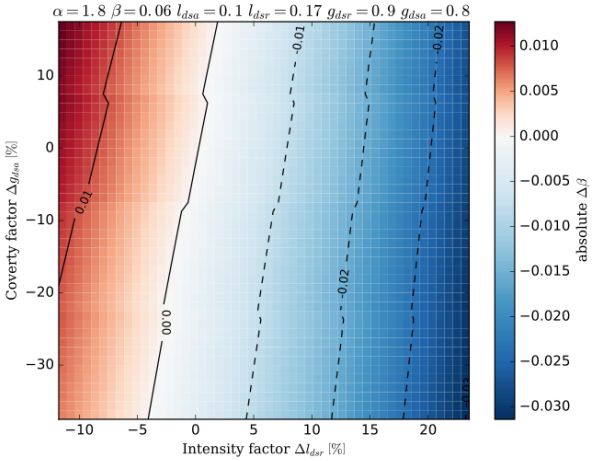

Figure 34: Variation of g_{dsa} has no significant influence of the turbidity retrieval. Consequently g_{dsa} can be set constant at a reasonable value.

4.2.4 Discussion

The sensitivity analysis of all three models provided information in how the parameters are correlated with each other and what accuracy can be expected facing a-priori estimation to reduce fitting parameters. The main goal is the determination of the aerosol parameters like Ångström exponent α, the turbidity coefficient β, the ozone scale height H_{oz} and water vapor wv. The Ångström exponent α is quite insensitive to the variation of the turbidity coefficient β and the coverty factor g_{dsa} which show strong correlations and a separation of the examined parameters via model inversion is difficult. Assuming the measurement data corresponds to the irradiance reflectance model α is possible within a certain area. Considering sky radiance model the intensity factor l_{dsr} can be retrieved reliable in with high accuracy below 1 % which serves as an input parameter for the sky radiance to downwelling irradiance reflectance. Besides this parameter

the ozone scale height H_{oz} and water vapor wv can be determined. For the sky radiance to downwelling irradiance reflectance l_{dsr} and the Ångström exponent α suit as reasonable input parameters to reduce fitting parameters. The parameter g_{dsa} has an low influence on the retrieval of the desired turbidity coefficient β thus it can be set to a constant value. In general the turbidity parameter β shows in all three models correlations with the corresponding aerosol scale factor like g_{dsa} and l_{dsa}. The sky radiance to downwelling irradiance reflectance shows less correlation thus a retrieval of the turbidity coefficient is possible.

4.3 Experimental Results

In this section the feasibility of the retrieval of atmospheric parameters based on the analytic radiate transfer model by Bird and Riordan [15] is analysed. At first the atmospheric parameter retrieval by means of inversion modelling is presented. Afterwards an overview of the test sites and the weather conditions are given which provide useful information for interpretation of the results and error discussion. At last the retrieved atmospheric parameters are validated against Microtops SolarLight and AERONET.

4.3.1 Parameter Retrieval

Measurements By inversion modelling the Ångström exponent α and turbidity coefficient β are retrieved. For this the total downwelling irradiance and the diffuse downwelling irradiance were measured via a spectralon of approximately 10 % reflectance (Figure 35). Figure 35a shows both total downwelling irradiance E_d, diffuse downwelling irradiance E_{ds} and the reflectance of both irradiances $\frac{E_{ds}}{E_d}$. The spectralon reflectance is not taken into account for these plots thus a factor of 10 has to be multiplied to receive the actual intensity of the detected signal. In Figure 35b the sky radiance in 0 ° zenith directions is shown. This plot shows clearly the absorption bands of H_2O and O_2.
The absorptive contribution cannot be neglected. This measurement was performed by holding the optics of the Ibsen spectrometer upside down. Dividing the sky radiance by the total downwelling irradiance results in the sky radiance to total downwelling irradiance reflectance $Lsky/E_d$ (see Figure 35c). The downwelling irradiance E_d is divided by the spectralon reflectance. In both reflectances it is clearly seen that the most absorptive spectral signature is eliminated by the division of both measurements. This is key idea of the measurement concept to ignore absorptive components and deduce the Ångström parameters by the radiance scattered by aerosol particles. As a consequence absorptive effects due to aerosols cannot be determined by means of presented retrieval but this can be neglected since in the visible spectrum process of light scattering dominate over process of absorption. The measurements shown in the in Figure 35a and Figure 35b were performed at an high zenith angle of $\approx$ 72°.

Model Inversion As described in section 3.3 the model inversion is performed by a nonlinear least-squared minimization. The used method ist the limited memory BFGS algorithm implemented in Python. GPS coordinates and UTC Time serves as input parameter to calculate the corresponding model. Three models for inversion modelling are implemented namely the irradiance reflectance $\frac{E_{ds}}{E_d}$, the sky radiance L_{sky} and the sky radiance reflectance in respective to the total downwelling irradiance $\frac{L_{sky}}{E_d}$. The parameter retrieval are obtained by fitting measurement set of Figure 35a. Hence good calibration and an exact model calculation are necessary requirements to perform the fit. In Figure 36 a fit of the irradiance reflectance $\frac{E_{ds}}{E_d}$ is presented with the corresponding residuals. The green error bars in the lower image represent the standard deviation of the measurement set performed at each time stamp. The standard deviation serves as weights for the model inversion. The residuals are not uniformly distributed around zero hence the models does not correspond exactly to the measurement data. Nevertheless the main goal is not the exact representation of the measured sky radiance data but to retrieve atmospheric parameters within a certain tolerance. In Figure 37 the fitting of the sky radiance in the region $350 - 400$ nm is presented to retrieve the intensity parameter l_{dsr}. Since the applied models are simplified analytic radiative transfer equations it is not necessary to resemble the exact spectral behavior of the sky radiance to retrieve the intensity parameter l_{dsr}.
The retrieval of the atmospheric parameters by applying the three models is described in section

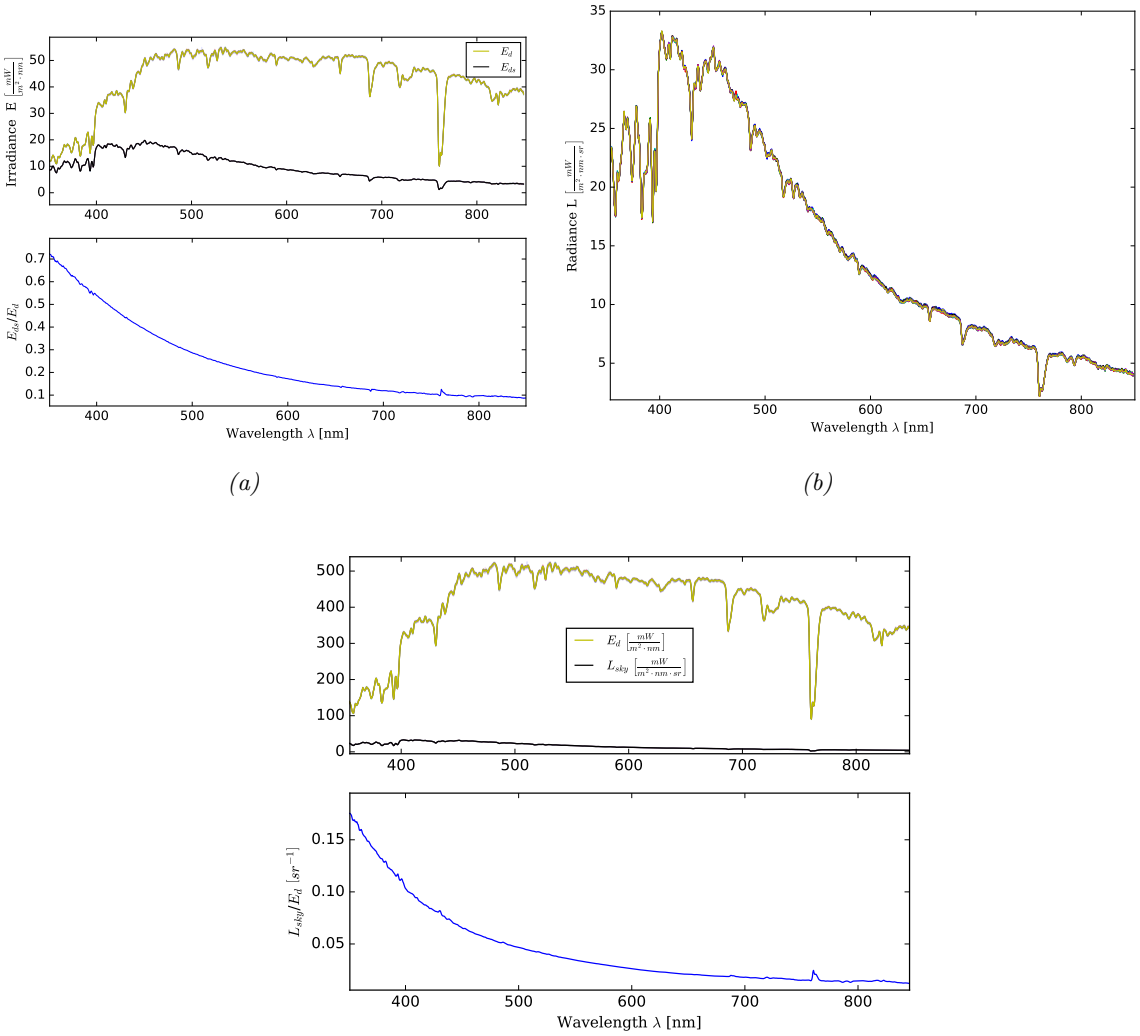

(a) *(b)* *(c)*

Figure 35: (a) The upper image represent the measured total downwelling irradiance and the diffuse irradiance. The lower image is the calculated reflectance of both measurements. The calculated reflectance is a smooth curve lacking of absorption bands. The radiance has to be multiplied by 10 according to the spectralon reflectance. (b) Sky radiance in 0 ° zenith directions. The absorption bands of H_2O *and* O_2 *are clearly visible. (c) The sky radiance in respective to the total downwelling irradiance are shown.*

4.2.4. The Ångström exponent α is obtained by the irradiance reflectance $\frac{E_{ds}}{E_d}$. If no sky radiance measurement is provided at the corresponding time stamp the turbidity parameter β is retrieved though the interpretation of these results must be treated with caution in view of high correlation. In case of an existing sky radiance measurement the intensity factor l_{dsr} is obtained by a fit in the shorter wavelength regime. Both retrieved parameters α and l_{dsr} serves as input parameter for the $\frac{L_{sky}}{E_d}$ model to retrieve the turbidity coefficient β. As discussed in 4.2.4 the value g_{dsa} is hold constant leaving for the fit only three parameters l_{dsa}, β and g_{dsr}. Additionally to the aerosol parameters the ozone scale height H_{oz} and the water vapor are determined by the sky radiance model. For the ozone scale height the wavelength range 540 - 640 nm is fitted and for water vapor the NIR regime 650 - 750 nm.

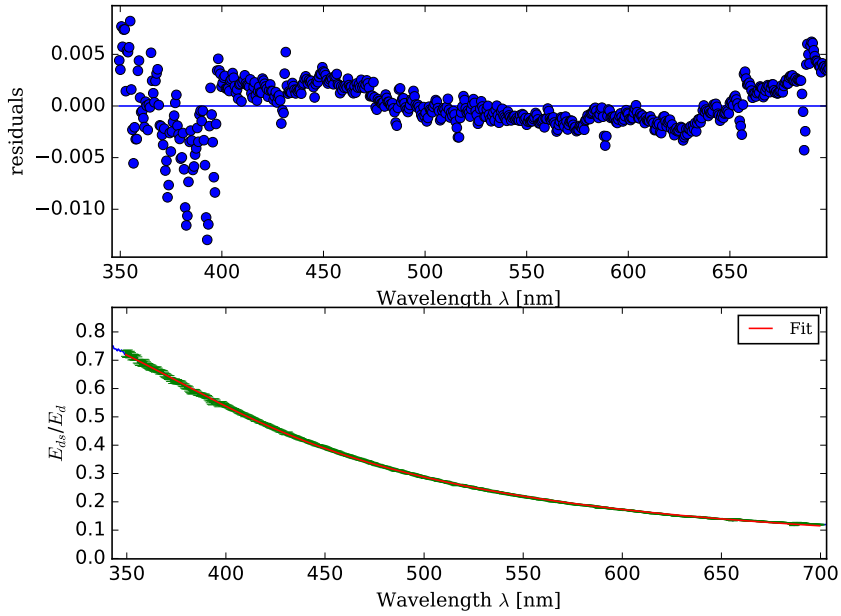

Figure 36: Fit of the irradiance reflectance $\frac{E_{ds}}{E_d}$. The measurements do have a higher standard deviation in the short wavelength regime which is taken into account for the model inversion. The irradiance reflectance fit does reach good convergence.

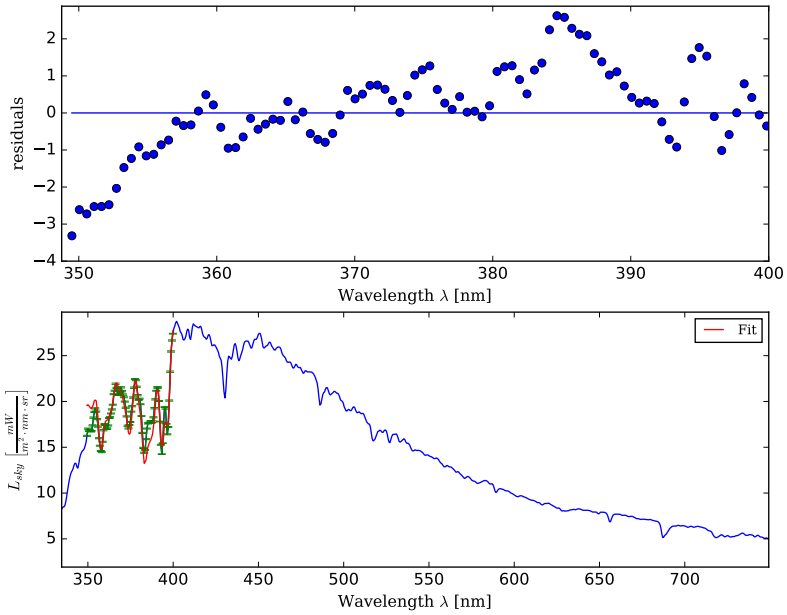

Figure 37: Fit of the sky radiance in the wavelength range 350-400nm. The residuals in the upper picture show that the model does not resemble the exact spectral behavior. Nevertheless this is not necessary to obtain the intensity factor l_{dsr} contributing to the Rayleigh scattering.

4.3.2 In-situ test areas

The set of measurements of the total downwelling irradiance, the diffuse downwelling irradiance and the sky radiance in 0 ° were taken place at five days. Since the model describes no scattering due to clouds excellent weather conditions with clear blue sky without any clouds formation were chosen (see Picture 40). The measurements were taken at two different sites.

- MIM: Lat: 48.148° , Longitude: 11.573°, elevation: 533.0 [m]
- DLR: Lat: 48.086° , Longitude: 11.273°, elevation: 490.0 [m]

Three measurements were taken on the roof of the Meteorological Institute Munich (MIM) at LMU Munich. This place was chosen to guarantee referenced AERONET Cimel sunphotometer which are installed on the roof. Two measurements were taken at the roof of the EOC building of DLR in Oberpaffenhofen. In Table 9 a list of the tests sites with the corresponding measurements and validation instruments is presented. Since these results were not performed in laboratory but on

Date	Irradiance Reflectance	Sky Radiance	SolarLight	AERONET	Location
29.11.2016	✓	✓	✓	✓	LMU
06.12.2016	✓	✓	×	✓	LMU
16.02.2017	✓	✓	✓	✓	LMU
13.09.2016	✓	×	✓	×	DLR
14.09.2016	✓	×	✓	×	DLR

Table 9: Experimental sites with corresponding measurements and validation instruments.

test sites under possible variable conditions and unknown sources of uncertainties it is important to take account for the current weather conditions, test surroundings and sun constellation to allow for interpretation of the in-situ measurement results. Weather stations nearby provide relative humidity for the test days (see Figure 38). Depending on chemical composition and size distribution the relative humidity changes the scattering enhancement of aerosol particles by taking up water. Thus their size distribution and chemical composition is changed. The effect of the relative humidity on the optical aerosol properties has been studied thoroughly [19, 62, 63]. The test surroundings were photographed to investigate the specific potential systematic error sources (see Figure 41). Moreover the current sun zenith angle depending on the observation position and the UTC Time were calculated. The most measurements were performed under high zenith angles thus high air masses (see Figure 39).

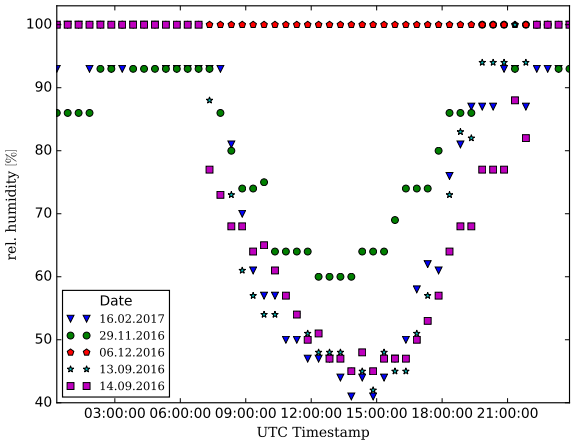

Figure 38: Relative humdity at measurement times corresponding to the specific measurement day.

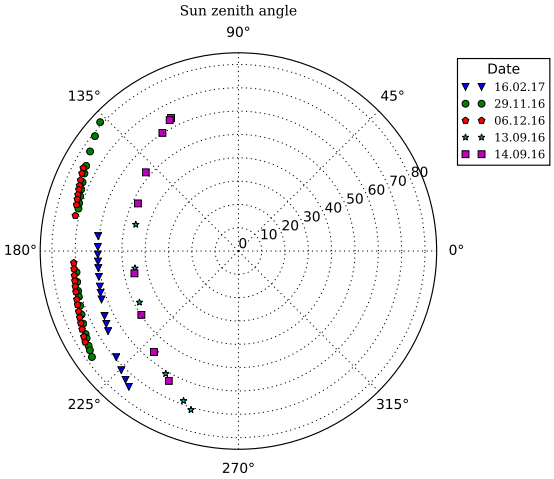

Figure 39: Sun zenith angle and elevation referring to the observer position at measurement times corresponding to the specific measurement day.

Figure 40: Measurement on the roof of the Meteorological Institute Munich (MIM) at LMU Munich. Clean sky conditions for aerosol parameter retrieval. The slight brightening of the sky radiance in direction to the horizon due to Rayleigh scattering can be clearly seen. February 16, 2017

Figure 41: Measurement of irradiance on the roof of the Meteorological Institute Munich (MIM) at LMU Munich (urban location). Surrounding causing neighbor effects and multiple scattering lead to possible biases in the retrieval of aerosol parameters.

4.3.3 Validation with AERONET and SolarLight

In the following figures the results of the Ångström exponent α and β in comparison to validation instruments are shown.

Ångström exponent: In Figure 42 the available validation instruments are the CIMEL sunphotometer of AERONET and the SolarLight Microtops Sunphotometer. The Ångström exponent α runs through the data points of AERONET at the first half of the day but seems to decrease monotonically for the second half of the day. Microtops data points do have an offset of -0.3 to the spectrometer values. Around 13:00 UTC Time the obtain parameters by Microtops sunphotometer shows outliers. The reason for these outliers can be deduced from the incorrect positioning of the sunphotometers during measurement time. For a good performance and to reduce measurement errors the sunphotometer have to be positioned horizontally with any tilting of the device. Consequently these values do not provide basis for comparison and might be excluded. The monotonically decreasing of the Ångström parameter is an interesting behavior which does appear in all measurement days (see Figure 43 and 44). The error bars are retrieved error bars of the fitting algorithm which is based on covariance matrix and have to be treated with caution since the fitting parameters are not uncorrelated. It has to be noticed that the error bars are estimated and dynamic and may not necessarily represent true uncertainties particularly for systematic errors in the measurement data. The Ångström parameters show the best results on the 29th, November and the 6th, December for the first part of the day. On 16, February α does not go through the points and is completely overestimated in comparison to AERONET and twice as high as the retrieved parameters of Microtops. By contrast the values of SolarLight Microtops are less than AERONET. On all measurement days the Ångström exponent obtained by the spectrometer are significantly higher than the values obtain by Microtops. At the test site DLR the monotonically decreasing is not observed for all measurement days.

Turbidity coefficient: The turbidity coefficient β retrieval appears to be challenging due to correlation with g_{dsa} and l_{dsa}. The starting points for the minimization algorithms have to be well chosen to guarantee reasonable results. This makes the retrieval less reliable. The best results are again on 29th, November. The retrieved parameters from the Ibsen spectrometer and the Microtops sunphotometer fluctuates around the AERONET data. This is not valid for the 6th, December and the 16, February. On 6th, December the values have a high fluctuation from 0.02 to 0.11. This deviation is due to the fact that β and l_{dsa} does compensate each other and a separation is not possible in respective to experimental data which contain unknown sources of uncertainties. At the test site of DLR Oberpaffenhofen the turbidity coefficient is retrieved from the $\frac{E_{ds}}{E_d}$ model. A reliable retrieval is thus not possible.

water vapor and ozone ... [64]

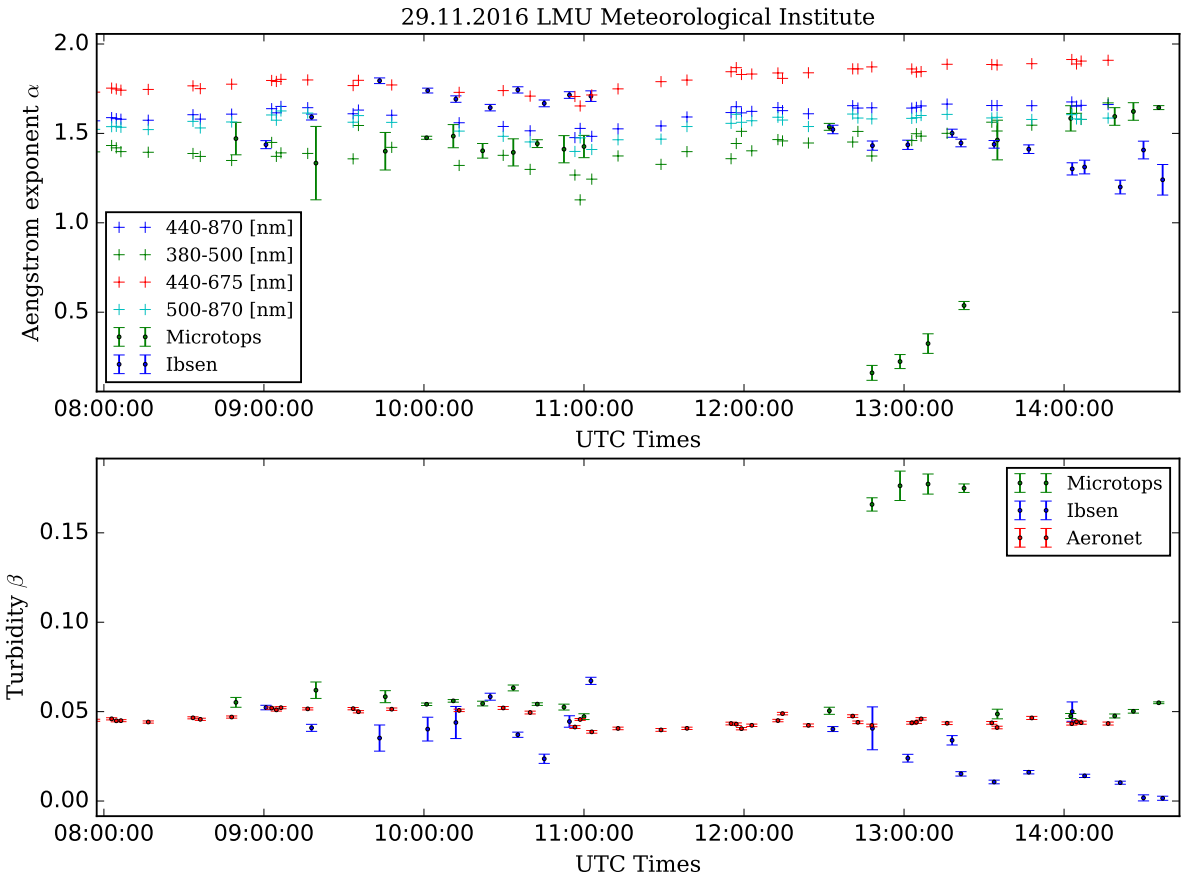

Figure 42: Retrieval of the Ångström exponent α and the turbidity coefficient β on the 29th, November. The Ångström exponent α of AERONET is divided in different wavelength regimes. The turbidity coefficient is calculated by the Ångström Formula with the obtained Ångström exponent and the aerosol optical depths.

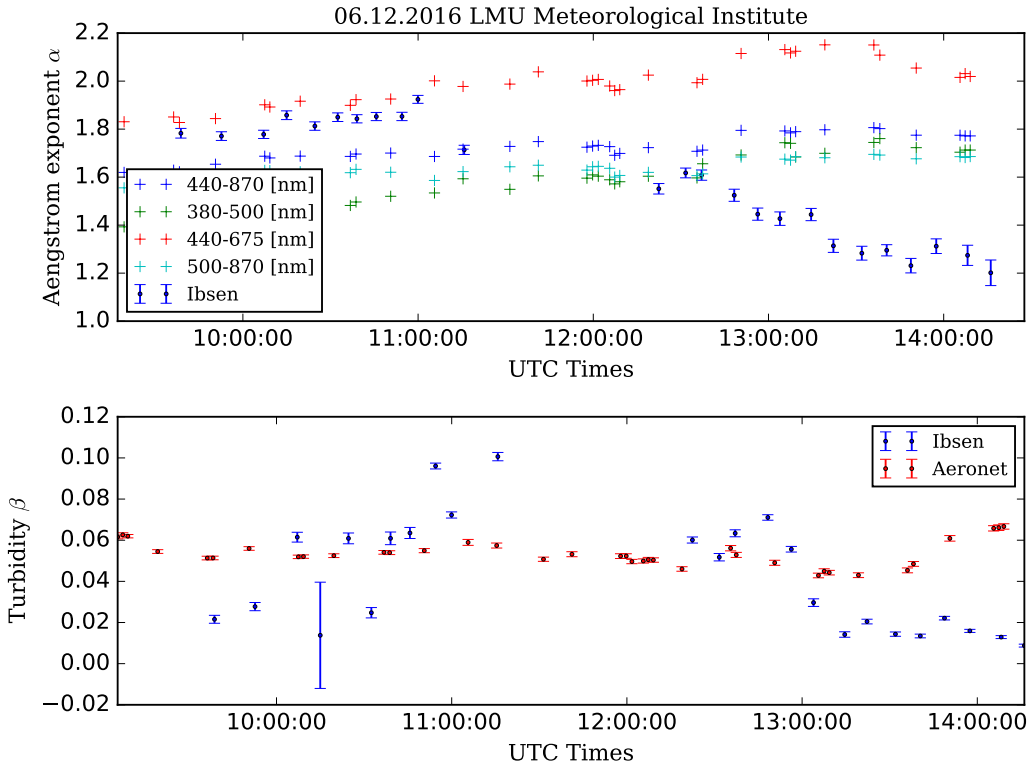

Figure 43: Retrieval of the Ångström exponent α and the turbidity coefficient β on the 6th, Dezember.

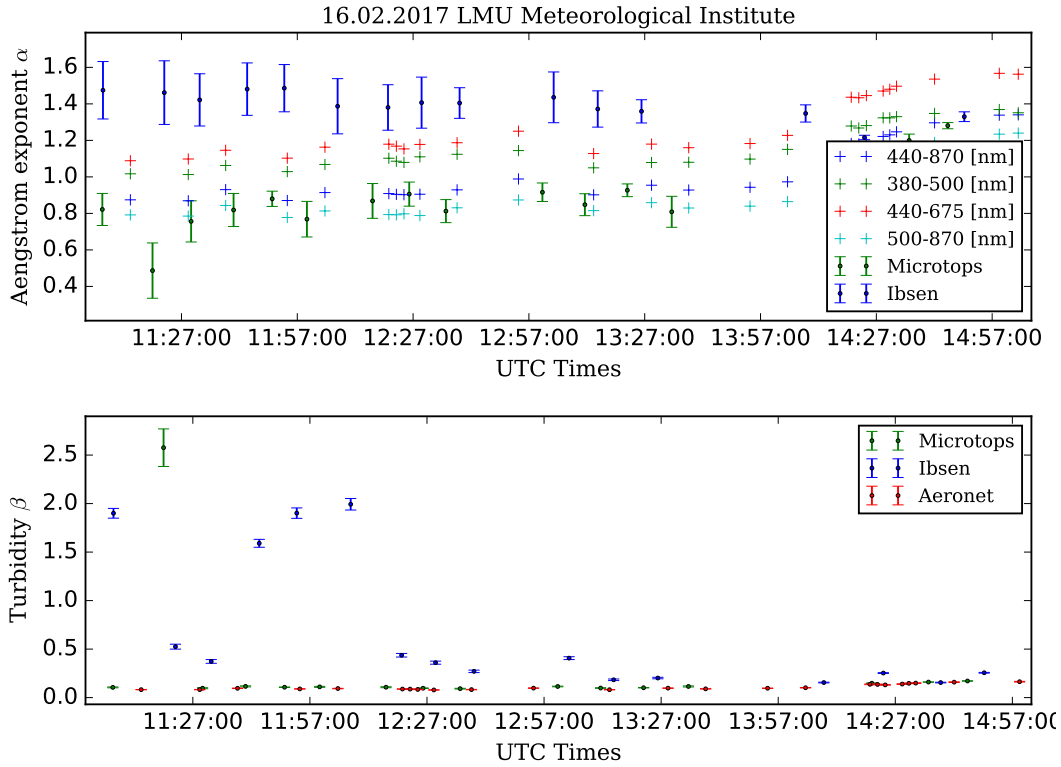

Figure 44: Retrieval of the Ångström exponent α and the turbidity coefficient β on the 6th, Dezember.

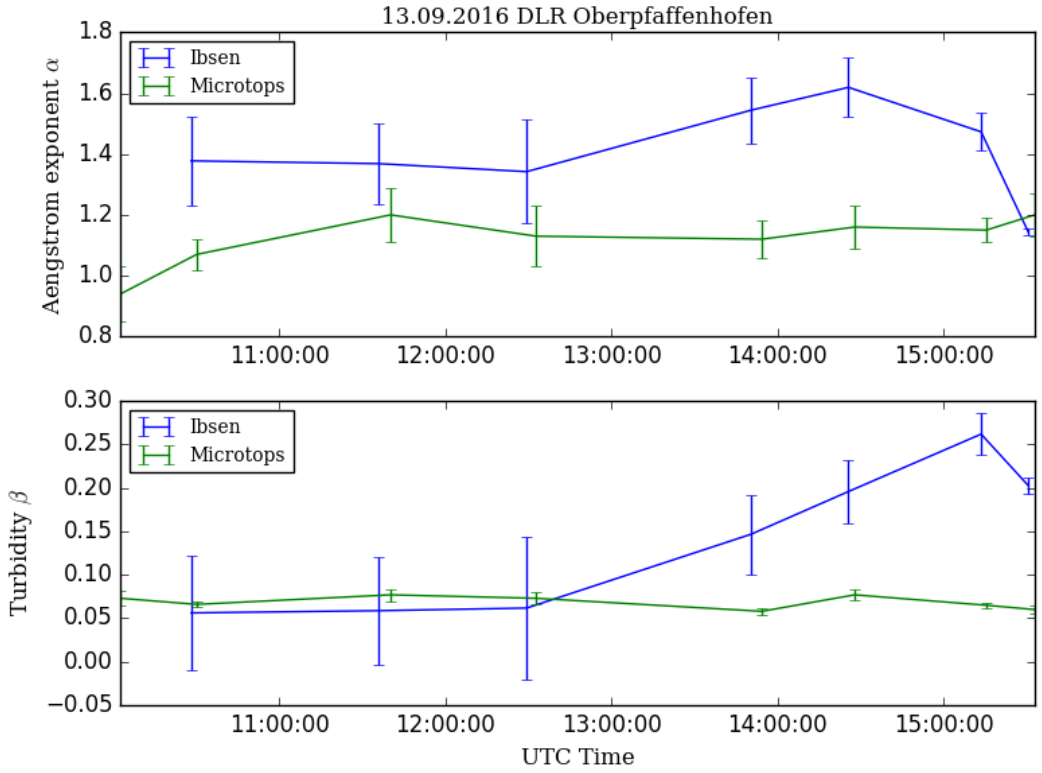

Figure 45: Retrieval of the Ångström exponent α and the turbidity coefficient β.

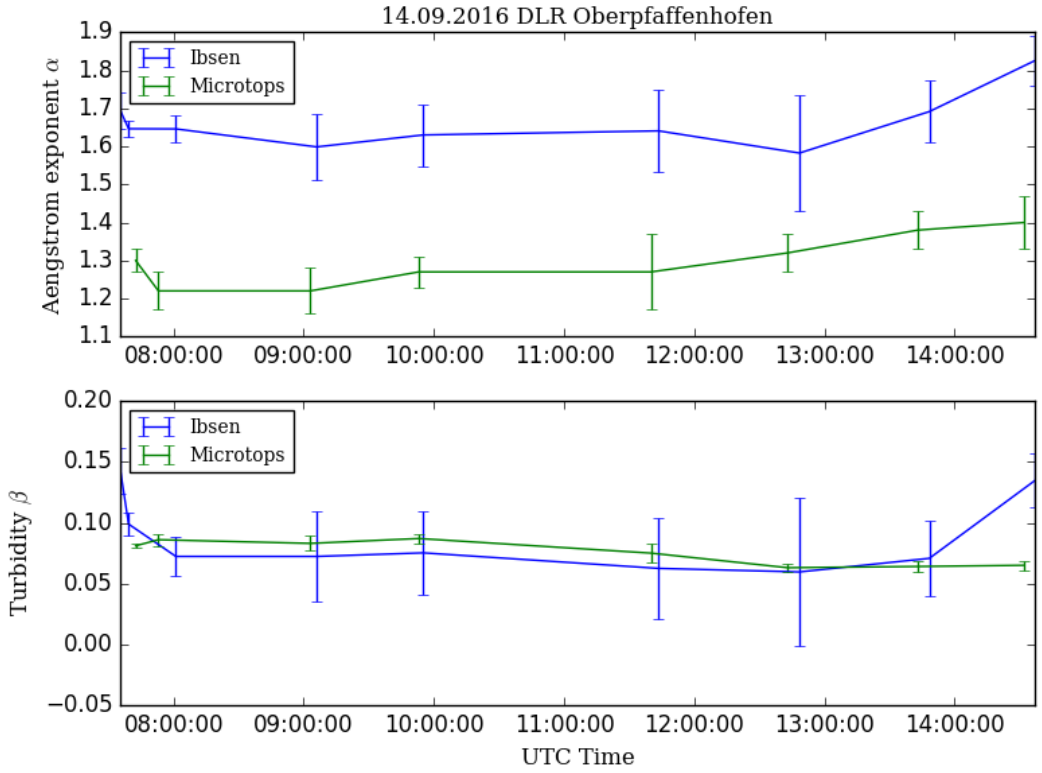

Figure 46: Retrieval of the Ångström exponent α and the turbidity coefficient β.

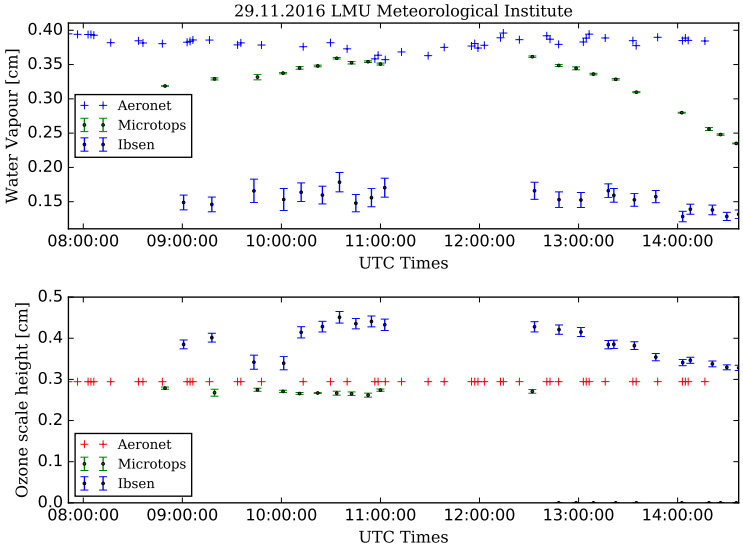

Figure 47: Water Vapor and Ozone

water vapour and ozone

4.3.4 Discussion

The retrieval of the Ångström exponent α shows satisfying results for the first half of the day on the 29th, November and on 6th, December. For these days the relative humidity was about 25 % higher than on 16th, February. Thus analyzing AERONET data of the 16th, February the Ångström exponent is relative low indicating a larger particle size of the aerosols. The lower relative humidity and the lower Ångström exponent confirms that urban aerosols mainly consists of water insoluble organics and soot and the scattering enhancement due to water uptake is low. The low Ångström exponent α and the trubidity coefficient β of about 0.1 cannot be retrieved reliably from the spectrometer measurements. The Ångström exponent from the spectrometer are mostly higher than retrieved Microtops II values. The increasing deviation of the values for the second half of the day may be caused by adjacency effects due to sun constellation in respective to the geometric setup. Figure 41 shows buildings and different instruments causing additional scattering of light. This would explain that this effect can be seen on the LMU but not on the roof of the DLR. Moreover a possible error source might be that during the diffuse sky radiance measurement a larger part around the sun is covered as it is intended. Due to the high zenith angles and the horizontal spectralon this seems obvious. Covering a larger part around the sun would cause to significant high errors due to the strong directional dependance of the phase function $P(\theta)$ of aerosols. This would explain the strong deviations on 16th, February where a low Ångström exponent is measured by AERONET and Microtops II indicating bigger particles and thus a stronger forward scattering. The retrieval of the turbidity coefficient is challenging considering the well chosen starting points for model inversion and the high correlation to l_{dsa} and g_{dsa}. Account for calibration errors and different error sources like adjacency effects it can be deduced that currently a reliable retrieval of the turbidity coefficient ist not possible. A recent study have shown that parallel measurements of sky radiances are highly sensitive to performed calibration procedures of the instruments and may result in differences of 5 - 35 % between sky radiances [65]. An active temperature stabilization for reducing thermal noise would lead to better and reliable results. It has to be considered that five measurement days is not representative to validate the presented method. Additional measurements on days with low

zenith angle should be performed to make a clear statement.

5 Summary and Conclusion

TODO brainstorm..

- impacts are most strongly felt on a regional scale
- complications arise due to the vertical homogeneity of the aerosol medium
- polarization

References

[1] IOCCG. Atmospheric correction for remotely-sensed ocean-colour products. *Reports of the International Ocean-Colour Coordinating Group*, 28(10), 2010.

[2] D. A. Siegel, M. Wang, St. Maritorena, and W. Robinson. Atmospheric correction of satellite ocean color imagery: the black pixel assumption. *Appl. Opt.*, 39(21):3582–3591, Jul 2000.

[3] Z. Mao, D. Pan, X. He, J. Chen, Ba. Tao, P. Chen, Z. Hao, Y. Bai, Q. Zhu, and H. Huang. A unified algorithm for the atmospheric correction of satellite remote sensing data over land and ocean. *Remote Sensing*, 8(7), 2016.

[4] E. Castillo-López, J. A. Dominguez, R. Pereda, J. M. de Luis, R. Pérez, and F. Piña. The importance of atmospheric correction for airborne hyperspectral remote sensing of shallow waters. application to depth estimation. *Atmospheric Measurement Techniques Discussions*, 2017:1–15, 2017.

[5] C. Mobley. The unsolved problem of atmospheric correction for airborne hyperspectral remote sensing of shallow waters. IOCCG Course, July 2014.

[6] `http://www.emceoc.org/atmospheric-correction.html`. [Online; accessed 2017].

[7] T. Evgenieva, I. Iliev, N. Kolev, P. Sobolewski, A. Pieterczuk, B. Holben, and I. Kolev. Optical characteristics of aerosol determined by Cimel, Prede, and Microtops II sun photometers over Belsk, Poland. 7027:70270V, December 2008.

[8] L. J. Bruce McArthur, David H. Halliwell, Ormanda J. Niebergall, Norm T. O'Neill, James R. Slusser, and Christoph Wehrli. Field comparison of network sun photometers. *Journal of Geophysical Research: Atmospheres*, 108(D19):n/a–n/a, 2003. 4596.

[9] P. Gupta S. More, P. Pradeep Kumar. Comparison of aerosol products retrieved from aeronet, microtops and modis over a tropical urban city, pune, india. *Aerosol and Air Quality Research*, 13(1):107–121, 2013.

[10] B.N. Holben, T.F. Eck, I. Slutsker, D. Tanré, J.P. Buis, A. Setzer, E. Vermote, J.A. Reagan, Y.J. Kaufman, T. Nakajima, F. Lavenu, I. Jankowiak, and A. Smirnov. Aeronet—a federated instrument network and data archive for aerosol characterization. *Remote Sensing of Environment*, 66(1):1 – 16, 1998.

[11] Norman T. O'Neill, A. Royer, and J. R. Miller. Aerosol optical depth determination from ground based irradiance ratios. *Appl. Opt.*, 28(15):3092–3098, Aug 1989.

[12] Global Aerosol Model Working Group. Guide: Guide to global aerosol models (gam) (aiaa g-065-1999). *American Institute of Aeronautics and Astronautics*.

[13] A. Kokhanovsky. *Aerosol Optics: Light Absorption and Scattering by Particles in the Atmosphere*. Springer Praxis Books. Springer Berlin Heidelberg, 2008.

[14] Murry L. S. *Physics of the Atmosphere and Climate*. Cambridge University Press, 2012.

[15] R.E. Bird and C. Riordan. Simple solar spectral model for direct and diffuse irradiance on horizontal and tilted planes at the earth's surface for cloudless atmospheres. *Technical Report*, 1984.

[16] P. Gege. Analytic model for the direct and diffuse components of downwelling spectral irradiance in water. *Appl. Opt.*, 51(9):1407–1419, Mar 2012.

[17] W. W. Gregg and K. L. Carder. A simple spectral solar irradiance model for cloudless maritime atmospheres. *Limnology and Oceanography*, 35(8):1657–1675, 1990.

[18] A. T. Young. Air mass and refraction. *Appl. Opt.*, 33(6):1108–1110, Feb 1994.

[19] E.P. Shettle, R.W. Fenn, and U.S. Air Force Geophysics Laboratory. *Models for the Aerosols of the Lower Atmosphere and the Effects of Humidity Variations on Their Optical Properties.* Environmental research papers. Optical Physics Division, Air Force Geophysics Laboratory, 1979.

[20] Garth W. Paltridge and C. Martin R Platt. *Radiative Processes in Meteorology and Climatology.* Developments in atmospheric science. Elsevier, 1976.

[21] A. Ångström. On the atmospheric transmission of sun radiation and on dust in the air. *Geografiska Annaler*, 11:156–166, 1929.

[22] A. Ångström. Techniques of determinig the turbidity of the atmosphere. *Tellus*, 13(2):214–223, 1961.

[23] H.S. Lim N.M. Saleh S.H. Chumiran A.N. Alias, M.Z. MatJafri and A. Mohamad. Inferring angstrom exponent and aerosol optical depth from aeronet. *Journal of Environmental Science and Technology*, 7:166–175, 2014.

[24] G. Gobbi, Y. Kaufman, I. Koren, and T. Eck. Classification of aerosol properties derived from aeronet direct sun data. *Atmospheric Chemistry and Physics*, 7(2):453–458, 2007.

[25] T. F. Eck, B. N. Holben, J. S. Reid, O. Dubovik, A. Smirnov, N. T. O'Neill, I. Slutsker, and S. Kinne. Wavelength dependence of the optical depth of biomass burning, urban, and desert dust aerosols. *Journal of Geophysical Research: Atmospheres*, 104(D24):31333–31349, 1999.

[26] N. T. O'Neill, T. F. Eck, B. N. Holben, A. Smirnov, O. Dubovik, and A. Royer. Bimodal size distribution influences on the variation of angstrom derivatives in spectral and optical depth space. *Journal of Geophysical Research: Atmospheres*, 106(D9):9787–9806, 2001.

[27] G. L. Schuster, O. Dubovik, and B. N. Holben. Angstrom exponent and bimodal aerosol size distributions. *Journal of Geophysical Research: Atmospheres*, 111(D7):n/a–n/a, 2006. D07207.

[28] C. Junge. The size distribution and aging of natural aerosols as determined from electrical and optical data on the atmosphere. *Journal of Meteorology*, 12(1):13–25, 1955.

[29] Michael D. King, Dale M. Byrne, Benjamin M. Herman, and John A. Reagan. Aerosol size distributions obtained by inversions of spectral optical depth measurements. *Journal of the Atmospheric Sciences*, 35(11):2153–2167, 1978.

[30] C.N. Davies. Size distribution of atmospheric particles. *Journal of Aerosol Science*, 5(3):293 – 300, 1974.

[31] C. F. Bohren and D. R. Huffman. *Absorption and scattering of light by small particles.* 1983.

[32] B. Castellani, E. Morini, M. Filipponi, A. Nicolini, M. Palombo, F. Cotana, and F. Rossi. Comparative analysis of monitoring devices for particulate content in exhaust gases. *Sustainability*, 6(7):4287–4307, 2014.

[33] L. G. Henyey and J. L. Greenstein. Diffuse radiation in the Galaxy. *Astrophysical Journal ApJ*, 93:70–83, January 1941.

[34] `http://earthobservatory.nasa.gov/Features/Aerosols/`. [Online; accessed 2017].

[35] H. Huang, G. E. Thomas, and R. G. Grainger. Relationship between wind speed and aerosol optical depth over remote ocean. *Atmospheric Chemistry and Physics*, 10(13):5943–5950, 2010.

[36] J.M. Ge, J. Su, Q. Fu, T.P. Ackerman, and J.P. Huang. Dust aerosol forward scattering effects on ground-based aerosol optical depth retrievals. *Journal of Quantitative Spectroscopy and Radiative Transfer*, 112:310–319, January 2011.

[37] U. Pöschl. Atmospheric aerosols: Composition, transformation, climate and health effects. *Angewandte Chemie International Edition*, 44(46):7520–7540, 2005.

[38] F. Immler, D. Engelbart, and O. Schrems. Fluorescence from atmospheric aerosol detected by a lidar indicates biogenic particles in the lowermost stratosphere. *Atmospheric Chemistry and Physics*, 5(2):345–355, 2005.

[39] Zhang R et al. Wang Y, Wang M. Assessing the effects of anthropogenic aerosols on pacific storm track using a multiscale global climate model. *Proceedings of the National Academy of Sciences of the United States of America*, 19:6894–6899, 2014.

[40] `http://www.dwd.de/EN/research/observing_atmosphere/composition_atmosphere/aerosol/cont_nav/particle_size_distribution_node.html`. [Online; accessed 2017].

[41] P. Koepke M. Hess and I. Schult. Optical properties of aerosols and clouds: The software package opac. *Bulletin of the American Meteorological Society*, 79(5):831–844, 1998.

[42] L. Bi, P. Yang, G. W. Kattawar, and R. Kahn. Modeling optical properties of mineral aerosol particles by using nonsymmetric hexahedra. *Appl. Opt.*, 49(3):334–342, Jan 2010.

[43] O. Dubovik, B. N. Holben, T. Lapyonok, A. Sinyuk, M. I. Mishchenko, P. Yang, and I. Slutsker. Non-spherical aerosol retrieval method employing light scattering by spheroids. *Geophysical Research Letters*, 29(10):54–1–54–4, 2002.

[44] C. Levoni, M. Cervino, R. Guzzi, and F. Torricella. Atmospheric aerosol optical properties: a database of radiative characteristics for different components and classes. *Appl. Opt.*, 36(30):8031–8041, Oct 1997.

[45] Solar Light Company Inc. *MICROTOPS II User's Guide Sunphotometer*.

[46] M. Morys, F. M. Mims, S. Hagerup, S. E. Anderson, A. Baker, J. Kia, and T. Walkup. Design, calibration, and performance of microtops ii handheld ozone monitor and sun photometer. *Journal of Geophysical Research: Atmospheres*, 106(D13):14573–14582, 2001.

[47] `https://aeronet.gsfc.nasa.gov/`. [Online; accessed 2017].

[48] T. Schwarzmaier, A. Baumgartner, P. Gege, C. Köhler, and K. Lenhard. The radiance standard rasta of dlr's calibration facility for airborne imaging spectrometers. In *SPIE Remote Sensing 2012*, pages 1–6, September 2012.

[49] K. Lenhard, A. Baumgartner, P. Gege, S. Nevas, S. Nowy, and A. Sperling. Impact of improved calibration of a neo hyspex vnir-1600 sensor on remote sensing of water depth. *IEEE Transactions on Geoscience and Remote Sensing*, 53(11):6085–6098, 2015.

[50] J. C. Dunlap, E. Bodegom, and R. Widenhorn. Nonlinear time dependence of dark current in charge-coupled devices. 7875:78750H, March 2011.

[51] P. Gege. Wasi-2d: A software tool for regionally optimized analysis of imaging spectrometer data from deep and shallow waters. *Computers and Geosciences*, 62:208 – 215, 2014.

[52] D.B.Allen A. Ingargiola M. Newville, T. Stensitzkil. LMFIT: Non-Linear Least-Square Minimization and Curve-Fitting for Python, September 2014.

[53] Richard H. Byrd, Peihuang Lu, Jorge Nocedal, and Ciyou Zhu. A limited memory algorithm for bound constrained optimization. *SIAM Journal on Scientific Computing*, 16(5):1190–1208, 1995.

[54] C. Ichoku, R. Levy, Y. J. Kaufman, L. A. Remer, R. Li, V. J. Martins, B. N. Holben, N. Abuhassan, I. Slutsker, T. F. Eck, and C. Pietras. Analysis of the performance characteristics of the five-channel microtops ii sun photometer for measuring aerosol optical thickness and precipitable water vapor. *Journal of Geophysical Research: Atmospheres*, 107(D13):AAC 5–1–AAC 5–17, 2002.

[55] T.A. Mather V.I. Tsanev. *Microtops Inverse Software Package for retrieving aerosol columnar size distributions using microtops II data.* Department of Chemistry, University of Cambridge, Department of Earth Sciences, University of Oxford.

[56] T. F.Eck O. Dubovik A.Smirnov, †B. N. Holben and I. Slutsker. Cloud-screening and quality control algorithms for the aeronet database. *Remote Sensing of Environment*, 73:337–349, 2000.

[57] Inversion product description. *AERONET Technical and Quality Assurance Documents.*

[58] M. Wendisch and W. Von Hoyningen-Huene. Possibility of refractive index determination of atmospheric aerosol particles by ground-based solar extinction and scattering measurements. *Atmospheric Environment*, 28(5):785 – 792, 1994.

[59] O. Dubovik and M. D. King. A flexible inversion algorithm for retrieval of aerosol optical properties from sun and sky radiance measurements. *Journal of Geophysical Research: Atmospheres*, 105(D16):20673–20696, 2000.

[60] O. Dubovik, A. Smirnov, B. N. Holben, M. D. King, Y. J. Kaufman, T. F. Eck, and I. Slutsker. Accuracy assessments of aerosol optical properties retrieved from aerosol robotic network (aeronet) sun and sky radiance measurements. *Journal of Geophysical Research: Atmospheres*, 105(D8):9791–9806, 2000.

[61] P. Gege. Sensitivity analysis of water depth determination. In *Ocean Optics XIX*, pages 1–11, October 2008.

[62] P. Zieger, R. Fierz-Schmidhauser, M. Gysel, J. Ström, S. Henne, K. E. Yttri, U. Baltensperger, and E. Weingartner. Effects of relative humidity on aerosol light scattering in the arctic. *Atmospheric Chemistry and Physics*, 10(8):3875–3890, 2010.

[63] P. Zieger, R. Fierz-Schmidhauser, E. Weingartner, and U. Baltensperger. Effects of relative humidity on aerosol light scattering: results from different european sites. *Atmospheric Chemistry and Physics*, 13(21):10609–10631, 2013.

[64] D. A. Jaffe and L. Zhang. Meteorological anomalies lead to elevated o3 in the western us in june 2015. *Geophysical Research Letters*, 2017. 2016GL072010.

[65] D. Pissulla, G. Seckmeyer, R. R. Cordero, M. Blumthaler, B. Schallhart, A. Webb, R. Kift, A. Smedley, A. F. Bais, N. Kouremeti, A. Cede, J. Herman, and M. Kowalewski. Comparison of atmospheric spectral radiance measurements from five independently calibrated systems. *Photochem. Photobiol. Sci.*, 8:516–527, 2009.